TANGO1 regulates membrane tension to mediate procollagen export

Ishier Raote[1], Maria F. Garcia-Parajo[2,3], Vivek Malhotra[1,3,4], and Felix Campelo[2]

[1] Centre for Genomic Regulation (CRG), The Barcelona Institute of Science and Technology, Barcelona, Spain.

[2] ICFO-Institut de Ciencies Fotoniques, The Barcelona Institute of Science and Technology, Castelldefels (Barcelona), Spain.

[3] Institució Catalana de Recerca i Estudis Avançats (ICREA), Barcelona, Spain.

[4] Universitat Pompeu Fabra (UPF), Barcelona, Spain.

Corresponding authors:

Felix Campelo

Tel: +34-93 554 2225

Fax: +34-93 553 4000

E-mail: felix.campelo@icfo.eu

Ishier Raote

Tel: +34-93 316 0187

Fax: +34-93 396 9983

E-mail: ishier.raote@crg.eu

ABSTRACT

The endoplasmic reticulum (ER)-resident transmembrane protein TANGO1 assembles into rings around COPII subunits at ER exit sites (ERES), and links cytosolic membrane-remodeling machinery, tethers, and ER-Golgi intermediate compartment (ERGIC) membranes to procollagens in the ER lumen (Raote *et al.*, 2018). This arrangement is proposed to create a direct route for transfer of procollagens from ERES to ERGIC membranes. Here, we present a physical model in which TANGO1 forms a linear filament that wraps around COPII lattices at ERES to stabilize the neck of a growing carrier on the cytoplasmic face of the ER. Importantly, our results show that TANGO1 can induce the formation of transport intermediates by regulating ER membrane tension. Altogether, our theoretical approach provides a mechanical framework of how TANGO1 acts as a membrane tension regulator to control procollagen export from the ER.

INTRODUCTION

Multicellularity requires not only the secretion of signaling proteins –such as neurotransmitters, cytokines, and hormones– to regulate cell-to-cell communication, but also of structural proteins such as collagens, which form basement membranes and more generally the extracellular matrix (ECM) (Kadler *et al.*, 2007; Mouw, Ou and Weaver, 2014). These extracellular assemblies of collagens are necessary for skin biogenesis and to form the connective tissues. ECM also likely acts as a ruler to control the size of a tissue. Collagens, like all secretory proteins, contain a signal sequence that targets their *de novo* synthesis into the endoplasmic reticulum (ER). After their glycosylation, folding and trimerization, the bulky procollagens are exported from the ER to the Golgi complex and thence to the exterior of the cells. The export domains of secretory cargoes, named the ER exit sites (ERES), are a fascinating subdomain of the ER, but the basic understanding of how these domains are created and segregated from rest of the ER for the purpose of cargo export still remains a major challenge. The discovery of TANGO1 as a key player that sits at ERES has made the process of procollagen export and the organization of ERES amenable to molecular analysis (Bard *et al.*, 2006; Saito *et al.*, 2009; Wilson *et al.*, 2011).

In the lumen of the ER, The SH3 domain of TANGO1 binds procollagen via HSP47 (Saito *et al.*, 2009; Ishikawa *et al.*, 2016) (***Figure 1A***). On the cytoplasmic side, TANGO1 has a proline-rich domain (PRD) and two coiled-coil domains (CC1 and CC2) (***Figure 1A***). The PRD of TANGO1 interacts with the COPII components Sec23A and Sec16 (Saito *et al.*, 2009; Ma and Goldberg, 2016; Maeda, Katada and Saito, 2017); the CC1 domain binds the NBAS/RINT1/ZW10 (NRZ) tethering complex to recruit ER-Golgi intermediate compartment (ERGIC) membranes (Santos *et al.*, 2015; Raote *et al.*, 2018); and the CC2 domain oligomerizes with proteins of the TANGO1 family (such as TANGO1 itself, the TANGO1-like protein cTAGE5, and the spliced isoform TANGO1-Short) (Saito *et al.*, 2011; Maeda, Saito and Katada, 2016; Raote *et al.*, 2018). Recently, we visualized procollagen export domains with high lateral spatial resolution using stimulated emission depletion (STED) nanoscopy in mammalian tissue cultured cells (Raote *et al.*, 2017, 2018). These studies revealed that TANGO1 organizes at the ERES into ring-like structures, of ~200 nm in diameter, that corral COPII components. Moreover, an independent study showed that TANGO1 rings are also present in *Drosophila melanogaster* (Liu *et al.*, 2017).

To further extend these findings, we combined STED nanoscopy with genetic manipulations and established that TANGO1 rings are organized by *(i)* lateral self-interactions amongst TANGO1-like proteins, *(ii)* radial interactions with COPII subunits, and *(iii)* tethering of small ER-Golgi intermediate compartment (ERGIC) vesicles to assist in the formation a procollagen-containing transport intermediate (Raote *et al.*, 2018). Overall, the accumulated data suggest a mechanism whereby TANGO1 assembles into a functional ring, which selectively gathers and organizes procollagen, remodels the COPII budding machinery, and recruits ERGIC membranes for the formation of a procollagen-containing transport intermediate. However, the biophysical mechanisms governing these events and how they are regulated by TANGO1 remain unknown.

Here, we present and analyze a biophysical model of TANGO1 ring assembly around polymerizing COPII-coated structures. Our model allows us to address: *(i)* the physical mechanisms by which TANGO1 and its interactors assemble into functional rings at ERES, forming a fence around COPII coat components; and *(ii)* how TANGO1 fence can couple membrane tension in

two compartments to modulate the formation of carriers at the ERES. Overall, we propose a novel mechanism of TANGO1-regulated procollagen export, which consists of two sequential steps. First, TANGO1 rings, at the edge of a polymerizing COPII structure, stabilize the neck of a growing procollagen-containing transport export intermediate and thus prevent premature carrier fission. Second, carrier growth can be stimulated by the ability of TANGO1 to act as a membrane tension regulator by tethering ERGIC membranes. Importantly, we show that TANGO1-mediated local reduction of the membrane tension at the ERES reduces the energy barrier required for carrier growth.

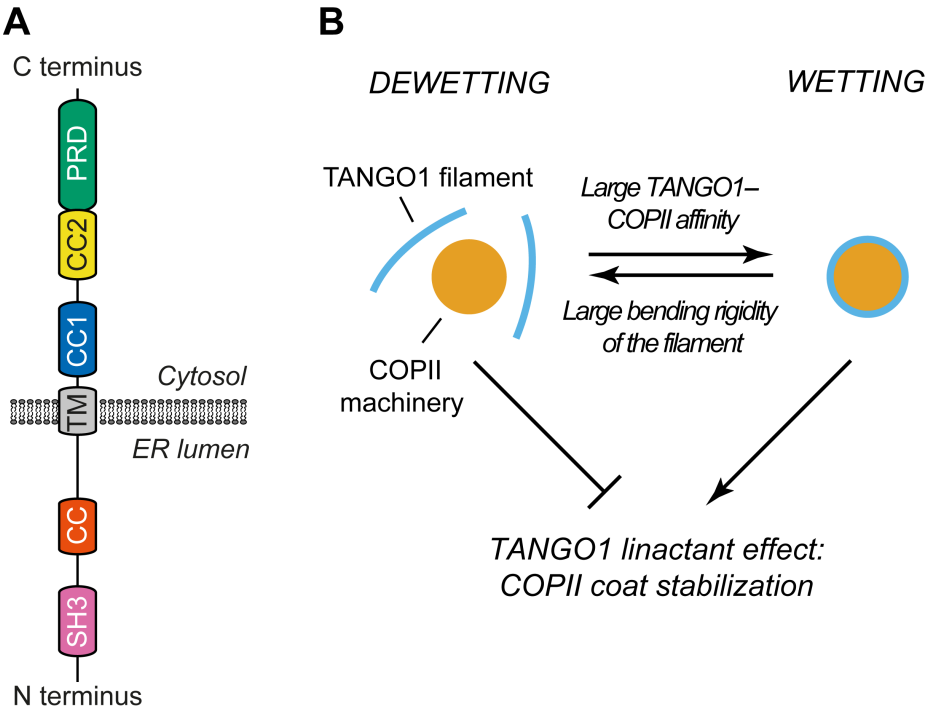

Figure 1. Qualitative description of the physical model of TANGO1 ring formation.
(A) Schematic representation of the domain structure and topology of TANGO1, indicating the SH3 domain, a luminal coiled-coiled domain (CC), the one and a half transmembrane region (TM), the coiled-coiled 1 (CC1) and 2 (CC2) domains, and the PRD. **(B)** Schematic description of the TANGO1 ring formation model. ERES consisting of COPII subunits assemble into in-plane circular lattices (orange), whereas proteins of the TANGO1 family assemble into filaments by lateral protein-protein interactions (light blue). A tug-of-war between the affinity of the TANGO1 filament to bind COPII subunits (promoting wetting) and the resistance of the filament to be bent (promoting dewetting) controls the wetting-dewetting transition. Only when TANGO1 wets the COPII lattice, it acts as a linactant by stabilizing the peripheral COPII subunits.

RESULTS AND DISCUSSION

PHYSICAL MODEL OF TANGO1 RING FORMATION

Experimental basis and assumptions of the model

To assess and rationalize the mechanisms by which TANGO1 assembles into rings at ERES, we propose a physical model built on accumulated experimental data.

First, we hypothesize that TANGO1 forms a filament that can be held together by lateral protein-protein interactions between TANGO1-family proteins (TANGO1, cTAGE5 and TANGO1-Short) (Raote *et al.*, 2018). This hypothesis is based on the following observations: *(i)* TANGO1 is seen in a ring-like filamentous assemblies by STED nanoscopy (Raote *et al.*, 2017); *(ii)* the direct 1:1 binding between TANGO1 and cTAGE5 CC2 domains (Saito *et al.*, 2011); *(iii)* the ability of TANGO1-Short and cTAGE5 to form oligomers and oligomeric complexes together with Sec12 and TANGO1 (Maeda, Saito and Katada, 2016); and *(iv)* the ability of TANGO1 and TANGO1-Short to directly homo-dimerize by their CC1 domains (Raote *et al.*, 2018). Such a filament would grow by the assembly of TANGO1-family proteins, which we propose to occur in a linear or quasi-linear fashion, thus forming a filament rather than a protein aggregate or protein cluster. From an elastic point of view, such a filament is subject to internal strains and stresses and therefore will resist bending away from its preferred shape or curvature. Evidence for the existence of linear assemblies of transmembrane proteins has indeed been reported in the context of transmembrane actin-associated (TAN) lines that couple outer nuclear membrane components to actin cables (Luxton *et al.*, 2010).

Second, we hypothesize that TANGO1 stabilizes the edges of the COPII lattice by reducing the line energy of the ERES (Glick, 2017). COPII coat assembly at the ERES occurs by polymerization of the individual COPII subunits into a lattice (Aridor, 2018). This process starts with activation and membrane binding of Sar1 GTPase, which recruits Sec23-Sec24 heterodimers that form the inner layer of the COPII coat. Subsequently, the second layer of the coat, composed of Sec13-Sec31 subunits, is recruited to the ERES, eventually leading to the budding of a COPII-coated vesicle. The free energy of coat polymerization includes the binding free energy of the COPII subunits, the elastic penalty of bending the membrane underneath, and also the line energy due to the unsatisfied binding sites of COPII subunits occupying the edges of the growing lattice. Because proteins of the TANGO1 family physically interact with the COPII components Sec23, Sec16, and Sec12, we argue that by binding to COPII subunits placed at the periphery of the growing coat (Ma and Goldberg, 2016; Hutchings *et al.*, 2018; Raote *et al.*, 2018), TANGO1 stabilizes the domain boundary, effectively reducing its line energy. In analogy to surfactants –molecules that adsorb into liquid-liquid two-dimensional interfaces decreasing their surface tension–, we propose that by binding to COPII subunits, TANGO1 proteins act as line-active agents, or *linactants* (Trabelsi *et al.*, 2008). In the context of HIV gp41-mediated membrane fusion, it has been shown that linactant compounds, such as vitamin E, lower the interfacial line tension between different membrane domains to inhibit HIV fusion (Yang, Kiessling and Tamm, 2016).

Third, we hypothesize that TANGO1 plays a role in regulating ERES organization and size through biochemical interactions that can alter the normal kinetics of COPII assembly and disassembly. Indeed, the self-assembly of COPII-coated domains or growing buds at the ERES is

a complex spatiotemporal dynamic process that involves GTP hydrolysis, protein turnover and diffusion, domain fusion, and transport carrier budding and fission events (Heinzer *et al.*, 2008). Remarkably, during this dynamic evolution, both the number and average size of ERES remain approximately constant (Bevis *et al.*, 2002): in normal conditions, mammalian cells display hundreds of ERES with diameters of about half a micron (Hammond and Glick, 2000; Farhan *et al.*, 2008; Heinzer *et al.*, 2008). Brownian dynamics simulations of a spatiotemporal model of ERES assembly indicated that the COPII turnover kinetics play a key regulatory role in controlling ERES size distribution (Heinzer *et al.*, 2008). Besides, those simulations also suggested a role for Sec16 in controlling the cooperative binding of COPII subunits to the ERES and thus in establishing their size distribution. We experimentally base our hypothesis on *(i)* the known interaction between TANGO1 and Sec16 (Maeda, Katada and Saito, 2017); *(ii)* the ability of cTAGE5 to recruit the Sar1 guanine-nucleotide exchange factor Sec12 (Saito *et al.*, 2014; Sasaki *et al.*, 2018); and *(iii)* the findings in *D. melanogaster* that loss of TANGO1 leads to smaller ERES, whereas its overexpression induces the formation of more and larger ERES (Liu *et al.*, 2017).

Formulation of a biophysical model for TANGO1 ring formation

Our model can be qualitatively described as a tug-of-war between different driving forces: the resistance to bending of TANGO1 filaments, the linactant effect of TANGO1 on COPII-coated ERES, and the TANGO1-mediated biochemical modulation of COPII dynamics. These different forces can favor, prevent, or modulate the formation of TANGO1 rings around COPII coats at ERES. For instance, if the resistance to bending of the TANGO1 filament is relatively small or the binding affinity of TANGO1 for the COPII subunits is relatively large, the filament will easily adapt its shape by wrapping around COPII patches forming a TANGO1 ring (a process we refer to as ERES *wetting*) (***Figure 1B***). As a result, there will be a linactant effect of TANGO1 on COPII-coated ERES that will reduce the line energy, thus limiting the growth of the ERES and the size of the TANGO1 rings (***Figure 1B***). By contrast, if TANGO1 filaments are very rigid or the affinity of TANGO1 proteins for COPII subunits is low (for instance, in cells expressing mutants of TANGO1 with reduced or abrogated interaction to COPII proteins), ERES wetting by the filament will be energetically unfavorable and as a results TANGO1 will not act as a COPII linactant (***Figure 1B***).

To quantitatively analyze this hypothesis, we start by considering a two-dimensional scenario where both TANGO1 filaments and COPII coats lie on the plane of a flat two-dimensional membrane (the role of the membrane curvature and the three-dimensional organization of the different molecular players to form a transport intermediate is described in the second part of this article). We use a coarse-grained, continuum model, which implicitly considers TANGO1 family proteins (TANGO1, cTAGE5 and TANGO1-Short) and TANGO1-binding COPII subunits. Here, the "microscopic" interaction energies are averaged out into "macroscopic" free energies, such as the filament bending energy, or the coat line energy. Although simplistic in nature, this continuum model is a suitable choice for a semi-quantitative description of the main physical mechanisms driving ring formation, as structural data on TANGO1 proteins are currently lacking.

For the sake of simplicity, we consider in our physical model that the ER membrane contains a certain number of independent, non-interacting COPII-enriched domains of radius R, distributed following a hexagonal array, with a center-to-center distance, a, between domains (***Figure S1A***). To understand the effect of proteins of the TANGO1 family on the size and shape of

COPII domains along the ER membrane, we need to consider the different protein interactions outlined above, namely *(i)* TANGO1-TANGO1 interactions, which control the bending energy of the TANGO1 filament; *(ii)* TANGO1 interaction with peripheral COPII subunits, which controls the line energy of the COPII domain; and *(iii)* TANGO1 interaction with regulatory COPII proteins, which controls COPII polymerization kinetics. In sum, the total free energy of the system is the addition of these different free energy terms (see ***Equations (M1–M4)*** in Materials and Methods, where a detailed mathematical description of the elastic model of TANGO1 ring formation is presented). We consider that the total surface area of our system and the total surface area covered by ERES is fixed, so instead of working with the extensive free energy of the system, F, we will work with the intensive free energy per unit ERES area, $f = F/A_{ERES}$. This free energy density for a system of circular domains of radius R can be represented as (see Materials and Methods)

$$f = \frac{\kappa_T \omega}{R}(1/R - c_0)^2 + \frac{2\lambda_0}{R}\left(1 - \frac{\Delta\lambda}{\lambda_0}\omega\right) + \frac{1}{2}f_0(R - R_0)^2, \qquad \textbf{(1)}$$

where ω is the wetting fraction, which represents the fraction of ERES boundary length associated with TANGO1 molecules; and R is the radius of the TANGO1 ring. The first term of ***Equation (1)*** represents the bending energy of the filament, and depends on two elastic parameters: the bending rigidity of the TANGO1 filament, κ_T, and the preferred curvature of the filament, c_0. The second term of ***Equation (1)*** represents the line energy of the COPII lattice, which depends on the COPII coat line tension in the absence of stabilizing TANGO1 molecules, λ_0, and on the COPII line tension reduction due to the linactant effect of TANGO1, $\Delta\lambda$. The third term of ***Equation (1)*** represents the phenomenological term associated with COPII assembly kinetics, which in turn depends on two phenomenological parameters: a coupling parameter, f_0, and a length scale, R_0 (see Materials and Methods for a detailed description of the model and the parameters). ***Equation (1)*** can be written by using dimensionless parameters as,

$$\bar{f} = \frac{\overline{\kappa_T}\omega}{\rho}(1/\rho - \bar{c_0})^2 + \frac{2}{\rho}\left(1 - \overline{\Delta\lambda}\omega\right) + \frac{1}{2}\bar{f_0}(\rho - 1)^2, \qquad \textbf{(2)}$$

where the dimensionless parameters are defined as $\bar{f} = \frac{f\lambda_0}{R_0}$, $\bar{f_0} = \frac{f_0 {R_0}^3}{\lambda_0}$, $\overline{\kappa_T} = \frac{\kappa_T}{{R_0}^2\lambda_0}$, $\bar{c_0} = c_0 R_0$, $\overline{\Delta\lambda} = \frac{\Delta\lambda}{\lambda_0}$, and $\rho = \frac{R}{R_0}$.

Elastic parameters of the ring assembly model

The free energy per unit area, ***Equation (1)***, depends on a number of physical parameters related to protein-protein interactions, namely the bending rigidity of the TANGO1 filament, κ_T; the preferred curvature of the filament, c_0; the line tension of the polymerizing COPII coat, λ_0; the line tension reduction of TANGO1, $\Delta\lambda$; and the phenomenological parameters, f_0 and R_0. The elastic parameters of the TANGO1 filament, κ_T and c_0, depend on the chemistry of the bonds between the different proteins within a TANGO1 filament. As we lack experimental data on the value of these parameters, we consider them within a wide range of reasonable values. Typical values of the bending rigidity of intracellular filaments, such as intermediate filaments, are of the order of $\kappa_{IF} = 2000\ pN \cdot nm^2$ (Fletcher and Mullins, 2010), which we consider as an upper limit for the rigidity of a TANGO1 filament. In addition, by taking $\kappa_T = 0$, we can exploit our model to study the case where TANGO1 proteins do not form a cohesive filament

by attractive lateral protein-protein interactions. The line tension of the polymerizing COPII coat, λ_0, has not been, to the best of our knowledge, experimentally measured. Nevertheless, the line tension of clathrin coats, which lead to the formation of vesicles of a size comparable to the standard COPII vesicles, has been recently measured, yielding a value of $\lambda_{clathrin} = 0.05\ pN$ (Saleem *et al.*, 2015). We use this value as a starting estimation, which we will vary within a certain range. Finally, the two phenomenological parameters can be related to each other and to the average size of ERES in stationary conditions, $R_{ERES} \sim 200\ nm$ (Heinzer *et al.*, 2008), as $R_0 = R_{ERES}\left(1 - \frac{2\lambda_0}{f_0 {R_{ERES}}^3}\right)$, implying that $0 \leq R_0 \leq R_{ERES}$ (see Supplementary Information).

A wetting-dewetting transition describes the formation of TANGO1 rings at ERES

ERES formation is a highly dynamic process, and once ERES are formed they are long-lived structures with a fast protein turnover (Forster *et al.*, 2006; Hughes *et al.*, 2009). Moreover, at steady state, an average number and size distribution of ERES is experimentally found (Hammond and Glick, 2000; Heinzer *et al.*, 2008). Hence, we considered that the steady-state average ERES size corresponds to the minimum of the total free energy of the system ***Equation (2)*** and determined the conditions promoting or preventing filament wrapping around COPII patches, which we refer to as ERES wetting. This configuration of minimal free energy is acquired by optimizing the free parameters of the model, namely the dimensionless size of the ERES, ρ, and the wetting fraction, ω.

Since the free energy in ***Equation (2)*** has a linear dependence on the wetting fraction, ω, it is monotonic with respect to this variable and therefore energy minimization will drive the system to either complete wetting ($\omega = 1$), or complete dewetting ($\omega = 0$), depending on the sign of $\partial \bar{f}/\partial\omega$. Hence, the wetting-dewetting transition corresponds, for a fixed value of the ERES size, to a stationary point of the free energy with respect to the wetting fraction, $\partial \bar{f}/\partial\omega = 0$. This condition sets a critical value of the TANGO1 line tension reduction, which defines the wetting-dewetting transition,

$$\overline{\Delta\lambda}^{wett} = \overline{\kappa_T}/2(1/\rho - \bar{c}_0)^2. \quad \textbf{(3)}$$

For $\overline{\Delta\lambda} > \overline{\Delta\lambda}^{wett}$, there is complete wetting of COPII domains by TANGO1 and thus full formation of TANGO1 rings; whereas for $\overline{\Delta\lambda} < \overline{\Delta\lambda}^{wett}$, there is dewetting and TANGO1 filaments are absent from COPII domains and no TANGO1 rings are formed (***Figure 2A***). Since the values of $\overline{\Delta\lambda}^{wett}$ are between 0 (no linactant effect) and 1 (full linactant effect), we can define a critical filament bending rigidity, $\bar{\kappa}^{dewett} = 2/(1/\rho - \bar{c}_0)^2$, above which there is complete dewetting of ERES by TANGO1 regardless of the value of $\overline{\Delta\lambda}$ (***Figure 2A***). Similarly, complete wetting occurs for any values of $\overline{\Delta\lambda}$ only if $\overline{\kappa_T} = 0$ or if $\bar{c}_0 = 1/\rho$ (***Figure 2A***).

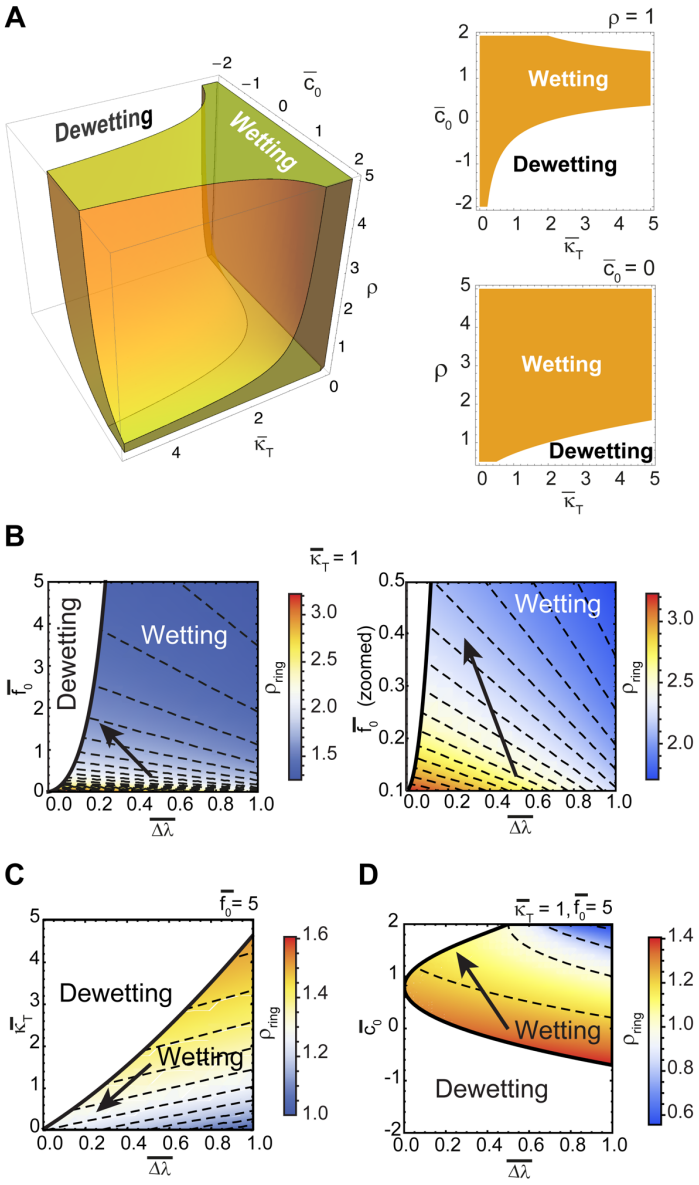

Figure 2. A wetting-dewetting transition controls the formation and size of TANGO1 rings. **(A)** Wetting-dewetting phase diagram. The three-dimensional diagram (left) indicates the region in the parameter space (orange region) where the system is under a wetting condition and hence TANGO1 rings surrounding ERES are to be expected. The diagram is shown as a function of the bending rigidity of the TANGO1 filament, $\overline{\kappa_T}$, the filament spontaneous curvature, $\overline{c_0}$, and the size of the ring, ρ, all in dimensionless units (see text). The right plots show cross-sections of the three-dimensional diagram at the indicated planes. **(B-D)** Numerically computed phase diagrams showing the wetting-dewetting transitions (solid black lines) as a function of the line tension reduction ($\overline{\Delta\lambda}$) and the dimensionless coupling factor, $\overline{f_0}$ **(B)**; the filament bending rigidity, $\overline{\kappa_T}$, **(C)**; or the spontaneous curvature, $\overline{c_0}$ **(D)**. The fixed parameters are indicated on the top part of the plots. In the parameter space where wetting is predicted, the optimal ring size, ρ_{ring}, is shown in color code. Dashed lines represent the iso-size lines, and arrows represent possible trajectories in the parameter space allowing for a reduction in the TANGO1 ring size while reducing affinity of TANGO1 filament for COPII subunits. In **(B)** we show the plots where the value of the coupling parameter, $\overline{f_0}$, takes a broad range of values (left graph), or a narrower, zoomed range of values (right graph). In **(B, C)** the filament spontaneous curvature is equal to 0.

Computation of the preferred size of TANGO1 rings

TANGO1 rings surround COPII components (Raote *et al.*, 2017), corresponding to a filament full wetting condition (that is, $\omega = 1$), as presented in ***Figure 1B*** (analysis of the ERES size in dewetting conditions is presented in the Supplementary Information). Under wetting conditions, a ring of radius R_{ring} is formed by a TANGO1 filament wrapping around a COPII patch. The value of the optimal dimensionless ring size, $\rho_{ring} = R_{ring}/R_0$, is obtained by minimizing ***Equation (2)*** in wetting conditions, which is equivalent to solve the fifth order algebraic equation,

$$\overline{f_0}\,\rho^4(\rho-1) - 2\left(1 - \overline{\Delta\lambda} + \frac{1}{2}\overline{c_0}^2\overline{\kappa_T}\right)\rho^2 + 4\overline{c_0}\overline{\kappa_T}\,\rho - 3\overline{\kappa_T} = 0. \qquad \textbf{(4)}$$

Because ***Equation (4)*** cannot be analytically solved, we opted to solve it numerically for different values of the model's parameters. As a starting point, we took the parameter values $\kappa_T = 500\ pN\cdot nm^2$ (corresponding to the TANGO1 filaments having a persistence length of $\xi_p \simeq 120\ nm$), $R_0 = 100\ nm$, $\lambda_0 = 0.05\ pN$ (see ***Table 1***), which yields $\overline{\kappa_T} = 1$. We then looked for the solutions of ***Equation (4)*** as a function of the dimensionless coupling parameter, $\overline{f_0}$, and of the relative line tension reduction, $\overline{\Delta\lambda}$. These results (***Figure 2B***), show that ring formation (wetting by the TANGO1 filament) can be induced by decreasing the coupling factor, $\overline{f_0}$, or by increasing the linactant strength of TANGO1, $\overline{\Delta\lambda}$. Since $\overline{\Delta\lambda}$ essentially corresponds to the COPII–TANGO1 binding affinity, and hence our results indicate that TANGO1 rings are stabilized by the association of TANGO1 proteins with peripheral COPII subunits. Furthermore, our results also show that the size of the TANGO1 rings decreases with increasing values of $\overline{\Delta\lambda}$, and with increasing values of $\overline{f_0}$ (***Figure 2B***). Next, we computed the wetting-dewetting diagram and the optimal TANGO1 ring size in wetting conditions as a function of the relative line tension reduction, $\overline{\Delta\lambda}$, and of the bending rigidity, $\overline{\kappa_T}$ (***Figure 2C, Figure S2A, B***), or the filament preferred curvature, $\overline{c_0}$ (***Figure 2D***, ***Figure S2D***), for fixed values of the dimensionless coupling parameter, $\overline{f_0}$. For completeness, in ***Figure S2***, we show some more examples of the computed values of the dimensionless ring size, ρ, as a function of a wide range of the parameters of our model, $\overline{f_0}$, $\overline{\kappa_T}$, $\overline{c_0}$, and $\overline{\Delta\lambda}$. Altogether, these results indicate that rings are smaller for large values of the linactant strength of TANGO1, $\overline{\Delta\lambda}$ (smaller effective line tension of the COPII lattice), for smaller values of the filament rigidity, $\overline{\kappa_T}$, and for larger (positive) values of the filament spontaneous curvature, $\overline{c_0}$ (***Figure 2B-D***). In other words, both a large affinity of TANGO1 proteins for COPII subunits and a small resistance of the TANGO1 filament to bending (which in structural terms can be thought of as a small lateral protein-protein interaction between the filament components) induce the formation of TANGO1 rings and tend to reduce the size of these rings.

Comparison with experimental results

We previously reported that cells expressing mutants of TANGO1 with abrogated binding to the COPII component Sec23 (TANGO1-ΔPRD mutant) present both smaller and less stable rings as compared to wild-type cells, including also the presence of some fused structures (Raote *et al.*, 2018). In cells expressing TANGO1-ΔPRD, the interaction between one of the filament components, TANGO1, and the COPII subunits is abolished, indicating that, although a TANGO1 filament could still be formed –this mutant does not alter the interaction between TANGO1 and other TANGO1 or cTAGE5 proteins (Raote *et al.*, 2018)–, the filament should be less line-active because the affinity to bind to the peripheral COPII subunits is reduced. In

this situation the filament proteins cTAGE5 (Saito *et al.*, 2011, 2014) and TANGO1-Short (Maeda, Saito and Katada, 2016) can still bind Sec23 and therefore reduce, albeit to a lesser extent than in wild-type cells, the COPII patch line energy. However, in our results presented in ***Figure 2B-D*** and ***Figure S2***, we observed that a reduction of the linactant strength of TANGO1 (parameter $\overline{\Delta\lambda}$) normally leads to an increase rather than a decrease of the ring size (see supplementary information for a more detailed discussion). To investigate how the lack of the PRD domain of TANGO1 contributes to form smaller rings, we explored how other differential properties of TANGO1-ΔPRD in relation to those of TANGO1-WT could lead to the experimentally-observed reduction in ring sizes from about 275±70 nm to 170±65 nm (mean Feret's diameter of the ring) (Raote *et al.*, 2018). Our model predicts that the experimentally observed reduction of TANGO1-ΔPRD ring size needs to parallel either *(i)* spatio-temporal regulation by the PRD of ERES dynamics (such as an increase in the parameter $\overline{f_0}$); *(ii)* a reduction of the filament bending rigidity, $\overline{\kappa_T}$; or *(iii)* an increase of the preferred curvature of the filament, $\overline{c_0}$ (***Figure 2B-D***, black arrows). The analysis of the conditions that can promote the assembly of fused TANGO1 rings, as experimentally observed in cells expressing the TANGO1-ΔPRD mutant (Raote *et al.*, 2018), is presented in Appendix 1. Taken together, our results highlight the dual function of the PRD of TANGO1, which on one hand reduces the ability of TANGO1 to wet the ERES, and on the other hand must control, according to the predictions of our model, filament physical properties and/or the spatio-temporal dynamics of ERES.

TANGO1 RINGS CAN HELP ASSEMBLE LARGE TRANSPORT INTERMEDIATES

Can TANGO1 modulate the shape of a growing bud to accommodate large and complex cargoes? And, if so, would the TANGO1 ring structure be especially suited to achieve this task? To answer these questions, we put together a physical model of transport intermediate formation that incorporates the effects of TANGO1 ring formation and wetting as discussed above. In our model, we consider different scenarios under which TANGO1 can modulate the standard spherical COPII carrier formation.

Qualitative description of TANGO1-mediated transport intermediate formation

The formation of the canonical coated transport carriers (such as COPI-, COPII-, or clathrin-coated carriers) relies on the polymerization of a large-scale protein structure on the membrane surface, the protein coat. Polymerized coats usually adopt spherical shapes, which bend the membrane underneath accordingly (Faini *et al.*, 2013). Membrane bending is promoted if the binding energy of the coat to the membrane is larger than the energy required to bend the membrane and if the coat structure is more rigid than the membrane (Kozlov *et al.*, 2014; Saleem *et al.*, 2015). Hence, in the absence of a functional TANGO1, COPII coats generate standard 60-90 nm spherical transport carriers (***Figure 3A***). In this situation, the neck of the growing carrier prematurely closes without being able to fully incorporate long semi-rigid procollagen molecules, which are not efficiently recruited to the COPII export sites due to the lack of TANGO1 (***Figure 3A***). In our model for TANGO1 ring formation, we proposed that one of the potential roles of such a ring is to act as a linactant to stabilize free COPII subunits at the edge of the polymerized structure (Glick, 2017; Raote *et al.*, 2017) and hence prevent or kinetically delay the premature closure of the bud neck (***Figure 3B***). Moreover, mechanical forces pointing to-

wards the cytosolic side of the bud, either from the ER lumen (e.g. TANGO1 pushing procollagen upwards) or from the cytosol (e.g. molecular motors pulling on the growing bud), will induce the growth of the transport intermediate (Derényi, Jülicher and Prost, 2002; Roux *et al.*, 2002; Koster *et al.*, 2003; Leduc *et al.*, 2004; Watson *et al.*, 2005; Pinot, Goud and Manneville, 2010) (***Figure 3C***). This pulling force can however be counterbalanced by membrane tension, which generally acts as an inhibitory factor preventing bud formation (Saleem *et al.*, 2015; Hassinger *et al.*, 2017; Wu *et al.*, 2017) (***Figure 3C***). At the same time, by its TEER domain, TANGO1 recruits the NRZ complex that tethers ERGIC53-containing membranes in apposition to TANGO1 rings (Raote *et al.*, 2018) (***Figure 3D***). Fusion of such vesicles to the budding site would deliver membrane lipids to the ER membrane, which rapidly and transiently induces a local drop in membrane tension, hence overcoming the tension-induced arrest in transport intermediate growth (***Figure 3E***). The shape and coat coverage of procollagen-containing export intermediates remain, to the best of our knowledge, a matter of speculation. Both long pearled tubes (***Figure 3E***) or long cylindrical vesicles have been proposed to function at the level of the ER membrane (Mironov *et al.*, 2003; Zeuschner *et al.*, 2006; Robinson *et al.*, 2015; Gorur *et al.*, 2017; Omari *et al.*, 2018; Yuan *et al.*, 2018). We recently proposed the alternative possibility that a short-lived, transient direct tunnel between the ER and the ERGIC/Golgi complex can allow for the directional export of cargoes from the ER (Raote and Malhotra, 2019). In our model, TANGO1 rings help prevent the fission of the carrier and thus allow for the formation of such tunnels between the ER and the ERGIC. Finally, COPII coats have a preference to polymerize into spherical structures, although there is experimental evidence of tubular COPII polymerization in vitro as observed by cryo-electron tomography (Zanetti *et al.*, 2013; Hutchings *et al.*, 2018).

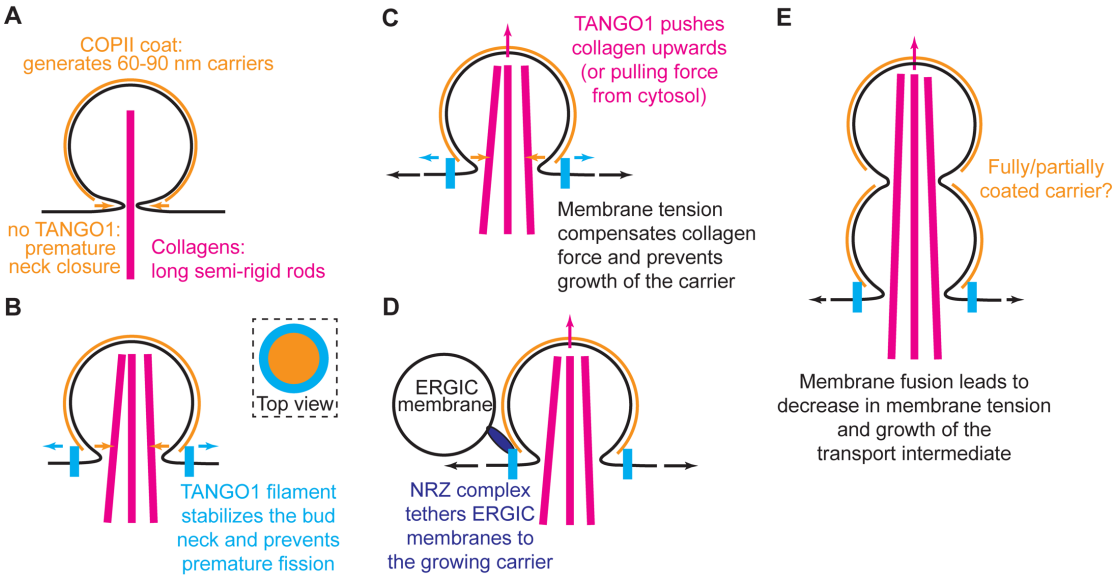

Figure 3. Physical model of how TANGO1 can regulate the formation of procollagen-containing transport intermediates.

(A) In the absence of functional TANGO1, COPII coated spherical vesicles assemble normally, generating spherical carriers of between 60–90 nm in size. Procollagens cannot be packed into such small carriers. **(B)** A TANGO1 filament siting at the base of a growing COPII patch encircles COPII components as experimentally observed (see top view in the top right subpanel) and packages procollagens to the export sites. This TANGO1 fence can serve to stabilize the neck of the transport carrier hence preventing the premature formation of a small carrier. **(C)** A possible cytosolically-directed force (procollagen pushing from the inside or a pulling force from the cytosol) can work in the direction of generating a long intermediate. By contrast, large membrane tensions work to prevent carrier elongation. **(D)** The NRZ complex,

which is recruited to the procollagen export sites by the TANGO1 TEER domain, tethers ERGIC53-containing membranes. **(E)** Fusion of these tethered membranes can lead to a local and transient decrease in the membrane tension, which can allow for the growth of the transport intermediate to be able to include the long semi-rigid procollagen molecules. Whether the intermediate is fully or only partially coated is still unknown.

Physical model of TANGO1-dependent transport intermediate formation

To quantitate the feasibility of the proposed pathway of transport intermediate growth (***Figure 3***), we developed a physical model that accounts for the relative contribution of each of these forces to the overall free energy of the system. Such a model allows us to predict the shape transitions from planar membrane to incomplete buds and to large transport intermediates. Intuitively, one can see that COPII polymerization favors the formation of spherical buds, whereas TANGO1 linactant strength and filament bending prevent neck closure. Large outward-directed forces promote the growth of long intermediates, whereas large membrane tensions inhibit such a growth. Taking advantage of a recently developed theoretical model of membrane elasticity in the context of clathrin-coated vesicle formation (Saleem *et al.*, 2015), we expand on this model to include the aforementioned contributions of TANGO1-like proteins in modulating COPII-dependent carrier formation. We consider that the ER membrane is under a certain lateral tension, σ_0, and resists bending by a bending rigidity, κ_b. Growth of a COPII bud starts by COPII polymerization into a spherical shape of radius R. The chemical potential of the COPII coat, μ_c, includes the COPII binding energy, ${\mu_c}^0$, and the bending energy of the underlying membrane (see Materials and Methods). As explained in the ring-formation model, incomplete buds are associated with a line tension of the free subunits, λ_0, which can be partially relaxed by the wetting of a TANGO1 ring, hence reducing the line tension by an amount $\Delta\lambda$. In addition, we also consider the chemical potential of the TANGO1 ring, μ_T, which accounts for the filament assembly energy via lateral interactions, ${\mu_T}^0$, and the filament bending energy. Next, we also account for the mechanical work of an outward-directed force, N, which favors transport intermediate growth. Finally, the fusion of incoming ERGIC53-containing membranes is accounted by a sharp and local reduction in the lateral membrane tension, by an amount equal to $\Delta\sigma$. Altogether, we can write the total free energy per unit surface area with respect to a naked flat membrane, f_c , as

$$f_c = \frac{(\sigma_0-\Delta\sigma)\,A_m-\left({\mu_c}^0-2\frac{\kappa_b}{R^2}\right)A_c+2\pi(\lambda_0-\omega\,\Delta\lambda)\,\rho-2\pi\left[{\mu_T}^0-\frac{\kappa_T}{2}\left(\frac{1}{R_T}-c_0\right)^2\right]R_T-Nh}{A_p}, \qquad \textbf{(5)}$$

where A_m is the membrane surface area, A_c is the surface area of the membrane covered by the COPII coat, A_p is the surface area of the carrier projection onto the flat membrane, ρ is the radius of the base of the carrier, h is the height of the carrier, and R_T is the radius of the TANGO1 ring (***Figure S3A***, and Materials and methods section). We consider that the carrier adopts the equilibrium configuration, corresponding to the shape of minimum free energy, ***Equation (5)***. Although the system is not in equilibrium, this assumption will be valid as long as the mechanical equilibration of the membrane shape is faster than the fluxes of the lipids and proteins involved in the problem (Sens and Rao, 2013; Campelo *et al.*, 2017). Hence, assuming local equilibrium, we calculated the shape of the carrier that minimizes ***Equation (5)*** under a wide range of possible values of the elastic parameters of the system (see Materials and methods). We define $\eta = h/2R$, which is the height of the carrier divided by the diameter of a fully formed bud, as a useful parameter to describe the shape of the transport intermediate. Taking

this into account, and assuming that the system has $n \geq 0$ fully formed buds, we can write down the free energy per unit area, ***Equation (5)***, as (see Materials and methods):

$$f_c = \begin{cases} \frac{\sigma-\tilde{\mu}}{1-\eta} + \frac{\tilde{\lambda}}{\sqrt{\eta(1-\eta)}} + \frac{\tilde{\kappa}_T}{[\eta(1-\eta)]^{3/2}}, & \eta < 1/2 \\ \sigma[1+4n+4(\eta-n)^2] - 4\tilde{\mu}\eta + 4\tilde{\lambda}\sqrt{(\eta-n)(1-\eta+n)} + \frac{4\tilde{\kappa}_T}{\sqrt{(\eta-n)(1-\eta+n)}}, & \eta > 1/2 \end{cases} \quad \textbf{(6)}$$

where $\tilde{\mu} = {\mu_c}^0 - 2\frac{\kappa_b}{R^2} + \frac{N}{2\pi R}$ is the effective chemical potential, which depends on the binding energy of the coat to the membrane, on the bending energy of the membrane, and on the applied pulling/pushing force; $\tilde{\lambda} = (\lambda_0 - \omega\,\Delta\lambda - {\mu_T}^0)/R$, is the effective line tension of the coat; and $\tilde{\kappa}_T = \kappa_T\omega/8R^3$ is the renormalized bending rigidity of the TANGO1 filament. From the expression for the effective chemical potential, $\tilde{\mu}$, we can see that the application of a force in the bud growth direction, N, plays the same role as the coat binding free energy, ${\mu_c}^0$, and therefore helps counterbalance the elastic resistance of the membrane to deformation. In addition, the lateral binding free energy of the TANGO1 filament, ${\mu_T}^0$, also helps, in wetting conditions, to decrease the value of the effective coat line tension, $\tilde{\lambda}$, thus preventing premature closure of the bud neck (***Figure 3***).

Functional TANGO1 rings can control transport intermediate formation by force exertion and membrane tension regulation

The free energy per unit area of the transport intermediate, f_c, has a non-trivial dependence on the shape of the carrier, parametrized by the shape parameter, η, as given by ***Equation (6)***. This implies that multiple locally stable shapes, corresponding to different local minima of the free energy, can coexist. To illustrate this dependence, the profile of the free energy per unit area, f_c, as a function of the shape parameter η, is shown for two different scenarios in ***Figure 4A***. In the first one, which corresponds to a situation where the COPII binding energy is relatively small, ${\mu_c}^0 = 0.012\ k_BT/nm^2$ (top panel, ***Figure 4A***), the global minimum of the free energy corresponds to a shallow bud. Other locally stable shapes, corresponding to a shallow bud connected to a set of spheres, can be found. By contrast, in the second scenario illustrated in ***Figure 4A*** (bottom panel), which corresponds to a situation of relatively large COPII binding energy, ${\mu_c}^0 = 0.048\ k_BT/nm^2$, the transport intermediate will grow from an initially unstable shallow bud (depicted in red, in ***Figure 4A***, bottom panel) to a locally stable almost fully formed spherical carrier (depicted in yellow, in ***Figure 4A***, bottom panel). Then, overcoming an energy barrier will result in further growth of the carrier into a large transport intermediate (depicted in green, in ***Figure 4A***, bottom panel). Next, we computed the profile of the free energy per unit area, f_c, as a function of the shape parameter η, for different values of the COPII binding energy, ${\mu_c}^0$, and of the TANGO1 bending rigidity, κ_T (***Figure 4B***). These results show that the bending rigidity of the TANGO1 filament, when assembled around the growing COPII bud, leads to the existence of a high energy barrier in the transition from a single bud to a multiple bud transport intermediate, or pearled tube (***Figure 4B***, compare dashed lines corresponding to a TANGO1 filament with no bending rigidity to the solid lines, where the TANGO1 filament is associated with a certain bending rigidity and therefore resists bending). A transition could still occur in this latter case, since the shape transition could occur through transient dewetting of the TANGO1 filament or through intermediate shapes between a cylindrical tube and a set

of spherical vesicles joined by a narrow connection, such as unduloids (see Materials and Methods).

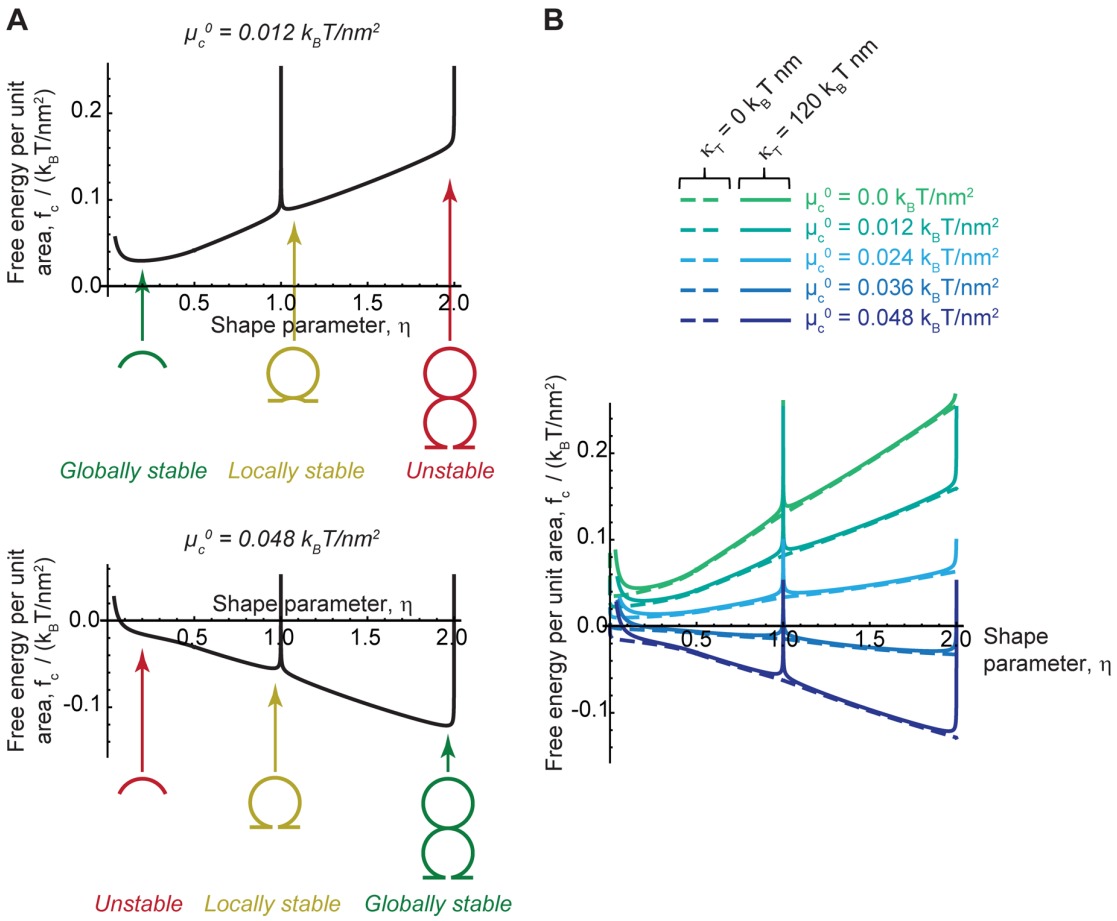

Figure 4. Free energy profile of a transport intermediate as a function of its shape.
(A) The free energy per unit area of the transport intermediate-TANGO1 system, f_c, plotted as a function of the shape parameter, η, for the COPII coat binding energy, $\mu_c^0 = 0.012\, k_BT\, nm^2$ (top plot), or $\mu_c^0 = 0.048\, k_BT\, nm^2$ (bottom plot). A schematic representation of the shape of the transport intermediate for different values of the shape parameter, η, is depicted, including locally stable shapes (in green), locally stable shapes (in dark yellow), as well as examples of unstable shapes (in red). **(B)** The free energy per unit area of the transport intermediate-TANGO1 system, f_c, plotted as a function of the shape parameter, η, for different values of the COPII coat binding energy, μ_c^0 (green-to-blue color-coded curves). The results are shown for the situation where we consider no TANGO1 filament (zero bending rigidity of the filament, $\kappa_T = 0$; dashed curves) and also for the situation where a TANGO1 filament is assumed (non-zero bending rigidity of the filament, $\kappa_T = 120\, k_BT\, nm$; solid curves).

We next looked for the locally and globally stable shapes of the transport intermediate, by computing the local minima of the overall energy of the system per unit area, ***Equation (6)***, for both single buds (shape parameter $\eta < 1$) or for long transport intermediates (shape parameter $\eta > 1$). In ***Figure 5***, we show, for a wide range of the model's parameters, the optimal shape of the intermediate, as measured by the optimal shape parameter, η^*, and the corresponding free energy per unit area for both single incomplete buds ($n = 0$; $\eta^* < 1$) (light blue lines in ***Figure 5***) and long intermediates containing one full bud plus an incomplete bud ($n = 1$; $1 < \eta^* < 2$) (orange lines in ***Figure 5***). Our results indicate that the rigidity of the TANGO1 filament has no effect on the shape of the transport intermediate and does not trigger the elongation of the

COPII bud (***Figure 5A***). When we varied the effective coat line tension, λ_{eff} (***Figure 5B***), we observed that for large values of the effective line tension, the shape of the intermediate tends to the complete bud ($\eta = 1$), but a transition to long pearled shapes is not promoted. In strong contrast, the COPII coat binding energy, ${\mu_c}^0$, does play an important role in controlling the elongation of the carriers, since our results (***Figure 5C***) show that increasing this value leads to a sharp transition from shallow buds (***Figure 5C***, top panel, solid blue line) to shallow pearled tubes (***Figure 5C***, top panel, solid orange line). Similarly, the application of a force directed towards the cytosol at the tip of the growing intermediate also leads to the transition from a shallow bud to a pearled tube (***Figure 5D***).

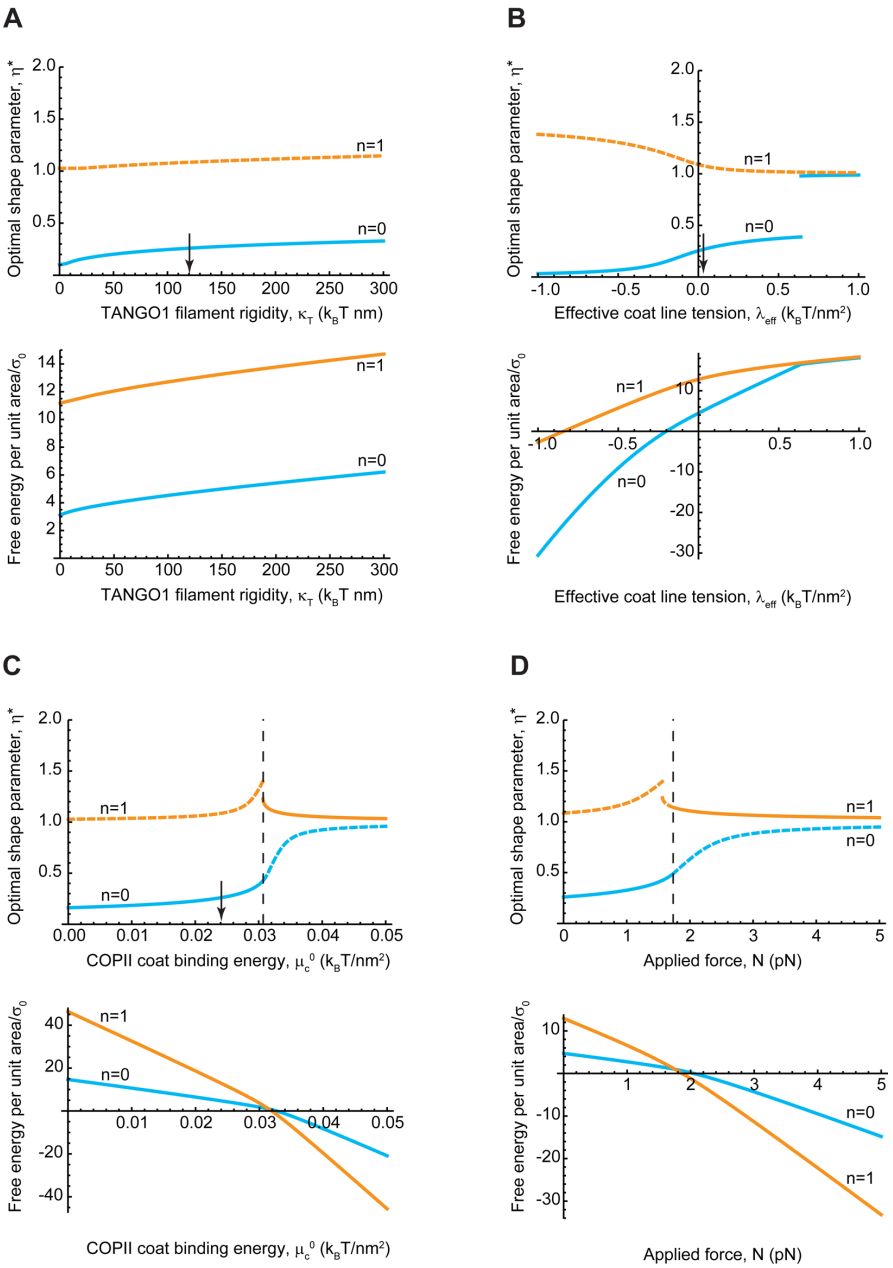

Figure 5. Shapes of the transport intermediates as a function of the different elastic parameters of the model.

(A) The optimal shape parameter, η^* (top graph), and the corresponding normalized free energy per unit area, f_c/σ_0 (bottom graph) are plotted as a function of the TANGO1 filament bending rigidity, κ_T, for incomplete buds ($n = 0$, blue curves) and for a long carrier consisting of one pearl and an incomplete bud

($n = 1$, orange curves). For this range of parameters the long carriers are of a higher energy than the incomplete buds, and hence they are metastable configurations (denoted by the dashed line in the top graph). **(B)** The optimal shape parameter, η^* (top graph), and the corresponding normalized free energy per unit area, f_c/σ_0 (bottom graph) are plotted as a function of the effective coat line tension, λ_{eff}, for incomplete buds ($n = 0$, blue curves) and for a long carrier consisting of one pearl and an incomplete bud ($n = 1$, orange curves). For this range of parameters, the long carriers are of a higher energy than the incomplete buds, and hence they are metastable configurations (denoted by the dashed line in the top graph). **(C)** The optimal shape parameter, η^* (top graph), and the corresponding normalized free energy per unit area, f_c/σ_0 (bottom graph) are plotted as a function of the COPII coat binding energy, μ_c^0, for incomplete buds ($n = 0$, blue curves) and for a long carrier consisting of one pearl and an incomplete bud ($n = 1$, orange curves). For this range of parameters, we observe a stability transition from incomplete buds to long carriers (denoted by the vertical black dashed line). In the top graph, we denote by solid and dashed lines in the top graph the stable and metastable configurations, respectively. **(D)** The optimal shape parameter, η^* (top graph), and the corresponding normalized free energy per unit area, f_c/σ_0 (bottom graph) are plotted as a function of the applied force, N, for incomplete buds ($n = 0$, blue curves) and for a long carrier consisting of one pearl and an incomplete bud ($n = 1$, orange curves). For this range of parameters, we observe a stability transition from incomplete buds to long carriers (denoted by the vertical black dashed line). In the top graph, we denote by solid and dashed lines in the top graph the stable and metastable configurations, respectively. The elastic parameters used for all the calculations shown in **(A-D)** are specified in ***Table 1***. Arrows in panels **(A-C)** indicate the standard parameters used to compute the complementary panels.

Next, we computed the transition zones as a function of the different parameters of the model (***Figure 6***). A three-dimensional phase diagram, shown in ***Figure 6A***, indicates the transitions from single incomplete buds to pearled tubes as a function of three parameters: the COPII coat binding energy, ${\mu_c}^0$; the applied force, N; and the membrane tension, σ. Remarkably, based on ***Equation (6)***, we can have a good analytical estimate of this transition zone, by considering the step-wise increase of the free energy (see Materials and methods), as

$$ {\mu_c}^0 - 2\frac{\kappa_b}{R^2} + \frac{N}{2\pi R} - \sigma_0 + \Delta\sigma = 0, \qquad (7) $$

which allows us to define a critical force $N^* = 2\pi R\left(\sigma_0 - \Delta\sigma - {\mu_c}^0 + 2\frac{\kappa_b}{R^2}\right)$; a critical coat binding energy, ${\mu_c}^{0^*} = \sigma_0 - \Delta\sigma + 2\frac{\kappa_b}{R^2} - \frac{N}{2\pi R}$; and a critical tension reduction, $\Delta\sigma^* = \sigma_0 - {\mu_c}^0 + 2\frac{\kappa_b}{R^2} - \frac{N}{2\pi R}$; above each of which the pearling transition is triggered. Taking the known or estimated parameters for the standard membrane tension of the ER, $\sigma_0 = 0.003\ k_BT/nm^2$ (Upadhyaya and Sheetz, 2004); for the membrane bending rigidity, $\kappa_b = 20\ k_BT$ (Niggemann, Kummrow and Helfrich, 1995); and for the size of the standard spherical COPII vesicle, $R = 37.5\ nm$ (Miller and Schekman, 2013); we get $\Delta\sigma^* = 0.031\ k_BT/nm^2 - {\mu_c}^0$, at zero force ($N = 0$); and $N^* = 7.4\ pN - {\mu_c}^0 \Big/ 0.0042\ k_BT/nm^2$ at no membrane tension reduction ($\Delta\sigma = 0$) (see ***Figure 6E***).

Taken together, the results we obtained from our physical model of large transport intermediate formation reinforce the notion that TANGO1 rings serve to control the growth of COPII carriers. TANGO1 rings can stabilize the COPII bud neck and thus prevent their premature closure by kinetically arresting or slowing down the completion of a spherical carrier. In such a situation, carrier expansion –according to the results of our model– can proceed via three different scenarios: *(i)* increase in the binding affinity of COPII coats to the membrane (***Figure 5C*** and

Figure 6); *(ii)* appearance of a directed force applied at the growing carrier and pointing towards the cytosol (***Figure 5D*** and ***Figure 6***); and *(iii)* local reduction of the membrane tension (***Figure 6***). TANGO1 can directly or indirectly control each of these possibilities (Ma and Goldberg, 2016; Raote *et al.*, 2018). Interestingly, the TANGO1 ring properties, such as the linactant power of TANGO1 or the TANGO1 filament bending rigidity, are not drivers of the incomplete bud to long transport intermediate transition (***Figure 6C,D***), but they seem to act more as kinetic controllers of the transition by preventing bud closure (***Figure 4***).

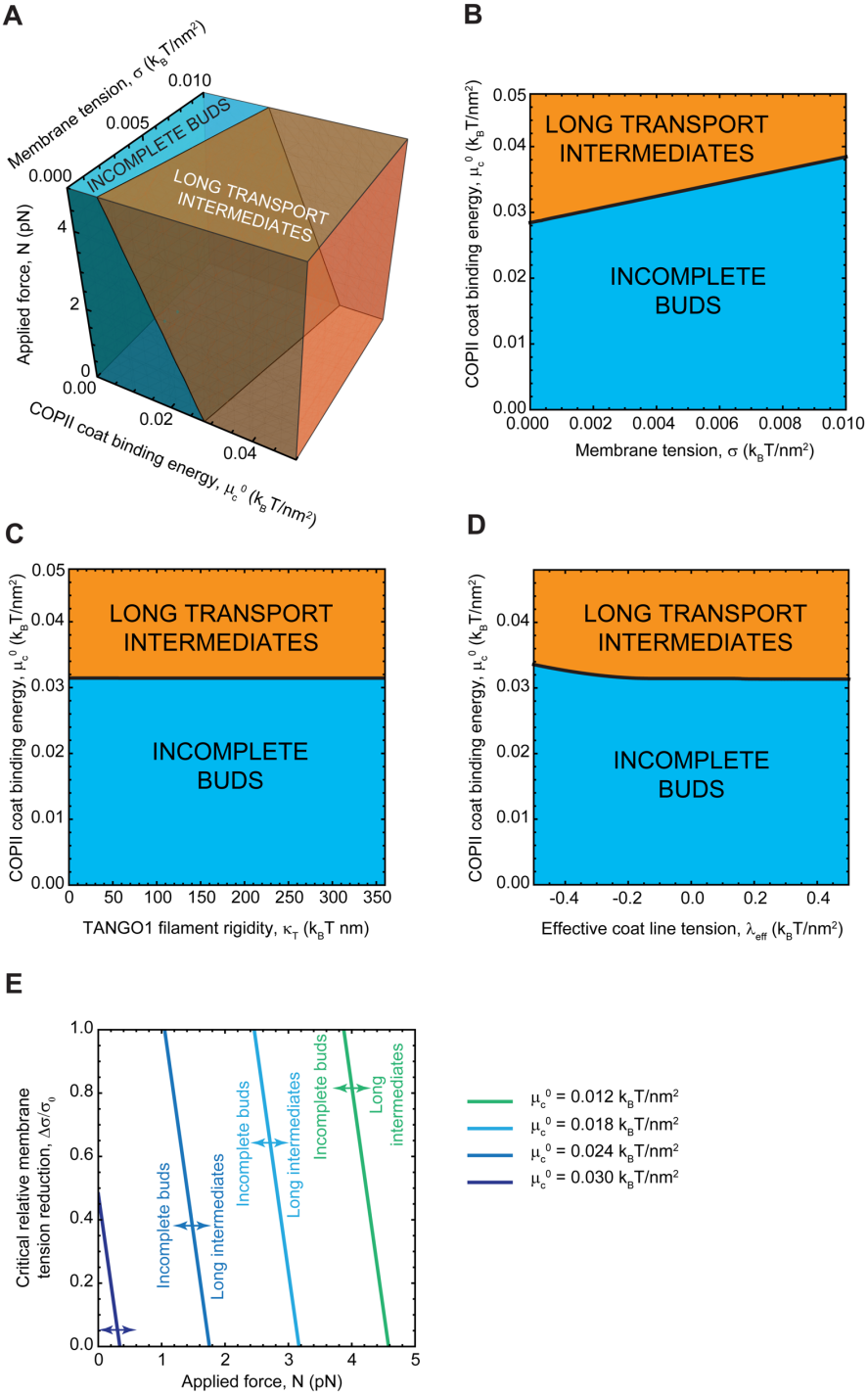

Figure 6. Shape diagram of the transport intermediate as a function of the TANGO1-controlled elastic parameters.

(A) Three-dimensional shape diagram indicating the shape of minimal elastic energy as a function of the COPII coat binding energy, μ_c^0, of the membrane tension, σ, and of the applied force, N. The region where incomplete buds correspond to the stable carrier shape is shaded in blue, whereas the region where long carriers ($n > 0$) correspond to the stable shapes is shaded in orange. **(B)** Two-dimensional cross-section of the shape diagram shown in **(A)** for vanishing applied force ($N = 0$). **(C)** Two-dimensional shape diagram as a function of the COPII coat binding energy, μ_c^0, and of the TANGO1 filament rigidity, κ_T, for vanishing applied force ($N = 0$) and a standard membrane tension, $\sigma = \sigma_0 = 0.003\ k_B T\ nm$. **(D)** Two-dimensional shape diagram as a function of the COPII coat binding energy, μ_c^0, and of the effective coat line tension, λ_{eff}, for vanishing applied force ($N = 0$) and a standard membrane tension, $\sigma = \sigma_0 = 0.003\ k_B T\ nm$. **(E)** The critical relative membrane tension reduction, $\Delta\sigma/\sigma_0$, above which the incomplete bud-to-long carrier transition is triggered, is plotted as a function of the applied force, N, for different values of the COPII coat binding energy, μ_c^0 (green-to-blue color-coded curves). Unless specified, the elastic parameters used for all the calculations shown in **(A-E)** are listed in ***Table 1***.

Proposal of experimental approaches to test our model

In this article, we proposed and analyzed a theoretical model to understand how TANGO1 molecules assemble into functional rings at the ERES, and how these rings can control the shape of transport intermediates. Our theoretical results will open up new avenues for experimental research on this topic and provide a common framework within which data and results can be understood. In particular, we envision that our work will stimulate future experimental efforts to test the proposed mechanisms of TANGO1-mediated ERES organization and collagen export. We propose here some possible routes by which the hypotheses and predictions of our model as well as some of the open questions it raised could be experimentally tested.

Does TANGO1 form a linear or quasi-linear filament held together by lateral protein-protein interactions? A first step to address this question will be to resolve the stoichiometry of the TANGO1 family proteins within a TANGO1 ring. Controlled photobleaching of the single-labeled, endogenously-expressed proteins (Lee *et al.*, 2012), would allow the recording of the number and spatial positions of single fluorophores in individual TANGO1 rings. These results, after complete quantitative reconstruction of all the single molecule signals, should provide an absolute stoichiometry and ultra-resolved structure of TANGO1 organization in the ERES. Ultimately, *in vitro* reconstitution of TANGO1 ring formation in synthetic lipid bilayers by using recombinant proteins will be of paramount importance to experimentally observe the formation of TANGO1 filaments, assess the minimal components required for their formation, and eventually measure the elastic properties of a TANGO1 filament.

Is tension homeostasis, controlled by TANGO1-directed fusion of incoming ERGIC membranes, a mechanism for transport intermediate formation? Future efforts in applying cutting-edge, super-resolution multicolor live-cell microscopy (Bottanelli *et al.*, 2016; Ito, Uemura and Nakano, 2018; Liu *et al.*, 2018; Schroeder *et al.*, 2019) will help monitor the fusion of ERGIC membranes to the ER and couple these events to the formation of procollagen-containing transport intermediates.

What can be the origin of the outwards-directed force driving transport intermediate elongation? It has been shown that procollagen export from the ER does not require the presence of an intact microtubule network (McCaughey *et al.*, 2019), however the involvement of other force-producing agents, such as actin-myosin networks, remains unknown. The identification of physiologically meaningful interactors of TANGO1 by proximity-dependent labeling assays, such as BioID (Roux *et al.*, 2018), and the subsequent screening for candidates that can exert

those forces would set the grounds to identify possible molecular players involved in force-generation.

Finally, what is the shape of the transport intermediate that shuttles collagens from the ER to the ERGIC/Golgi complex? To this end, three-dimensional, multicolor super-resolution microscopy techniques, such as 3D single molecule localization microscopy (3D-SMLM) or 3D stimulated emission depletion (3D-STED) microscopy, could provide sufficient resolution to map the three-dimensional morphology of the transport intermediates. Recent efforts by using 3D-SMLM and correlative light and electron microscopy (CLEM) have revealed the existence of large procollagen-containing structures (Gorur *et al.*, 2017; Yuan *et al.*, 2018). However, further work is needed to ascertain if these structures are indeed transport-competent carriers. By contrast, direct transport of procollagen between the ER and the Golgi complex by a short-loop pathway in the absence of large vesicles has been recently proposed (McCaughey *et al.*, 2019), opening to the possibility of a direct tunneling mechanism for trafficking proteins between compartments (Raote and Malhotra, 2019). Eventually, the use of modern electron microscopy techniques such as cryo-electron tomography (Beck and Baumeister, 2016) or focused ion beam-scanning electron microscopy (FIB-SEM) (Nixon-Abell *et al.*, 2016) will help solve this issue on the morphology of the transport intermediates that shuttle procollagens form the ER to the Golgi complex.

TANGO1 as a regulator of membrane tension homeostasis

We previously showed that TANGO1 forms circular ring-like structures at ERES surrounding COPII components (Raote *et al.*, 2017). We also revealed the interactions that are required for TANGO1 ring formation, which are also important to control TANGO1-mediated procollagen export from the ER (Raote *et al.*, 2018). However, it still remained unclear whether and how TANGO1 rings could organize and coordinate the budding machinery for efficient procollagen-export. Here, we proposed, described, and analyzed a feasible biophysical mechanism of how TANGO1 mediates the formation of procollagen-containing transport intermediates at the ER. The general idea backed by the results of our model is that TANGO1 rings serve as stabilizers of small buds, preventing the premature formation of standard COPII coats. TANGO1 is ubiquitously expressed in mammalian cells, including cells that secrete very low amounts of collagen. Furthermore, TANGO1 resides in most ERES in all these different cell lines, yet small COPII-coated vesicles form normally in those sites. How can this be understood? We propose that the ability of TANGO1 to form rings around COPII subunits is a first requirement for TANGO1 to promote procollagen export in non-standard COPII vesicles. Accumulations of export-competent procollagen at the ERES could re-organize the TANGO1 molecules laying there into functional rings surrounding COPII components and kinetically preventing the formation of small COPII carriers. Tethering of ERGIC53-containing vesicles mediated by the TANGO1 TEER domain (Raote *et al.*, 2018) could be the trigger to allow for carrier growth. Importantly, the ER-specific SNARE protein Syntaxin18 and the SNARE regulator SLY1, which together trigger membrane fusion at the ER, are also required for procollagen export in a TANGO1-dependent manner (Nogueira *et al.*, 2014). Fusion of ERGIC membranes to the sites of procollagen export would lead to a local and transient reduction of the membrane tension, which can promote, according to our theoretical results, the growth of the COPII carrier. In this scenario, TANGO1 would act as a regulator of membrane tension homeostasis to control procollagen export at the ERES. In parallel, we can also foresee a situation by which TANGO1 rings help pushing procollagen molecules into the growing carrier and couple this pushing force to procollagen folding, through the chaperone HSP47 (***Figure 3***). This pushing force, according

to our model, would also promote the formation of a large intermediate and hence TANGO1 could act as a sensor of procollagen folding to couple it with the export machinery.

What controls the organelle size in the context of intracellular trafficking? There has been a lot of work on what set the size of organisms, the size of tissues in an organism, and the size of cells in a tissue. However there has been relatively less work on the question of what sets the size of organelles relative to the cell. Extensive cargo transfer while trafficking bulky cargoes such as collagens leads to large amounts of membrane being transferred from organelle to organelle. To maintain organellar homeostasis, loss of membrane from a compartment has to be concomitantly compensated by membrane acquisition from the biosynthetic pathway or by trafficking from other organelles; the arrival and departure of membrane at each compartment has to be efficiently balanced. How is this homeostatic balance controlled? Changes in membrane tension have been described to affect rates of exocytosis and endocytosis at the plasma membrane (Apodaca, 2002; Kosmalska *et al.*, 2015; Wu *et al.*, 2017). Interestingly, a theoretical model has also established a crucial role for membrane tension in modulation the transition to bud clathrin-coated vesicles (Hassinger *et al.*, 2017). However, control of endomembrane trafficking by membrane tension is more challenging to study experimentally and hence still remains poorly understood. We propose that TANGO1 serves as a hub in the ER to connect different organelles for the intracellular traffic by controlling the tension homeostasis and regulating the membrane flux balance between these organelles.

In summary, we proposed a theoretical mechanical model that explains how TANGO1 molecules form functional rings at ERES, and how these TANGO1 rings assemble the machinery required to form a large transport intermediate commensurate to the size of procollagens. We envision that our hypotheses and the predictions of our model will open up new lines of experimental research to help understand how COPII coats organize together with proteins of the TANGO1 family to allow for the export of folded procollagen out of the ER.

MATERIALS AND METHODS

DETAILED DESCRIPTION OF THE PHYSICAL MODEL OF TANGO1 RING FORMATION

TANGO1 filaments are described by their physical length, L_T, which is proportional to the number of protein monomers forming the filament; and by their persistence length, $\xi_p = \kappa_T/k_BT$, –where κ_T is the filament bending rigidity and k_BT is the thermal energy, equal to the Boltzmann constant times the absolute temperature (Doi and Edwards, 1986)–, which describes how stiff the filament is. As long as the filament length is not much larger than the persistence length, the bending energy of the TANGO1 filament can be expressed as $F_{bend} = \frac{\kappa_T}{2}\int_{L_T}(c - c_0)^2 dl$, where c and c_0 are the actual and spontaneous curvature of the filament, respectively, and the integral is performed over the entire filament length. We define positive spontaneous curvatures of the filament as those where the TANGO1-COPII interacting domains lie on the concave side of the filament, and negative when they lie on the convex side. For a system of n circular domains of radius R, the filament bending energy can be written as

$$F_{bend} = n\pi\kappa_T\omega R(1/R - c_0)^2, \qquad \textbf{(M1)}$$

where we assumed that any existing filaments not adsorbed to the COPII patches adopt the preferred curvature, and where ω is the wetting fraction: the fraction of domain boundary length covered ("wetted") by TANGO1 molecules. The chemical potentials of free (not filament-associated) and of bound (filament-forming) TANGO1 proteins are, respectively, $\mu_f = {\mu_f}^0 + k_BT\log c_f$, and $\mu_b = {\mu_b}^0$. Here, ${\mu_f}^0$ and ${\mu_b}^0$ are the standard chemical potentials, which include the enthalpic contributions to the free energy per molecule, and define the energy of monomer binding to the filament, $\varepsilon_b = {\mu_b}^0 - {\mu_f}^0 < 0$; and the logarithmic term takes into account the contribution of the translational entropy. In addition, transient breakage of the filament (either stochastic or assisted) exposes free filament ends, which carry an extra energy due to the unsatisfied bonds, each of which contributes with an amount equal to ε_b. In principle this filament free-end energy could be different for each of the members of the TANGO1 family, however, for the sake of simplicity, we consider them all to be equivalent to each other. We will only need to take into account this energy term when considering interactions between neighboring rings, which involve a partial breakage of otherwise closed filaments (see Appendix 1).

Second, the effect of COPII polymerization on the ER membrane has two contributions on the total free energy of the system: the first one is through the line tension, λ_0, of a COPII-coated membrane patch; and the second one is associated to the chemical potential of COPII polymerization, μ_0. The line energy of such a domain can be expressed as $F_{line} = \lambda_0 L$, where L is the domain length. We allow for the possibility that TANGO1 proteins, upon adsorbing to the boundary of the COPII domains by binding the most external subunits, effectively decrease the line tension of the COPII domain to a new value $\lambda' = \lambda_0(1 - \Delta\lambda/\lambda_0)$, where $\Delta\lambda/\lambda_0$ is the relative decrease in the line tension, a measure of the linactant power of TANGO1. Altogether, we can write the line energy term as

$$F_{line} = \lambda_0\left(1 - \frac{\Delta\lambda}{\lambda_0}\omega\right)L. \qquad \textbf{(M2)}$$

If the system is composed of n circular domains of radius R, covering a total ERES surface area of $A_{ERES} = \pi n R^2$, then the total boundary length is $L = 2\pi n R$. The free energy term contributed by the chemical potential of polymerization is

$$F_{pol} = -\mu_0 A_{ERES}, \qquad \textbf{(M3)}$$

which describes, by classical nucleation theory, a minimum ERES size, $R_{min} = \lambda'/\mu_0$, above which the polymerizing domain is stable and can dynamically grow (Frolov *et al.*, 2006).

And third, we need to include an extra energy term, F_{phen}, which includes all the factors that modulate the domain size distribution, including the aforesaid chemical potential of COPII polymerization (Heinzer *et al.*, 2008). This phenomenological free energy term, F_{phen}, should have a local minimum at certain domain size, $R_0(\omega)$, which could in principle change by the presence of TANGO1 and hence depend on the wetting fraction, ω. For the sake of simplicity, we will disregard this dependence, and consider R_0 as a free parameter in our model. Hence, we can approximately express this free energy as a phenomenological free energy term for a system of n domains as a second order series expansion around this minimum as

$$F_{phen} = \frac{1}{2} f_0 (R - R_0)^2 A_{ERES}, \qquad \textbf{(M4)}$$

where f_0 is a coupling factor that dictates the strength of the phenomenological free energy with respect to the rest of factors the overall system free energy. Notice that we decoupled the line energy of the domain, Eq. **(M2),** from this phenomenological energy. This phenomenological approach is in some aspects akin to the Ginzburg-Landau theory of phase transitions (Foret, 2005; Wolff, Komura and Andelman, 2015; Schmid, 2017), where a phenomenological free energy is proposed as a function of an order parameter, which plays the role of the local concentration of coat subunits on the membrane, and includes a homogeneous term (usually a bistable potential), which plays the role of our F_{phen}, ***Equation (M4)***; and a gradient penalty, which plays the role of the line energy, ***Equation (M2)***.

The effects of other known players, such as the complex spatiotemporal dynamics of ERES components, the recruitment of ERGIC53-positive membranes by TANGO1, and the recruitment of procollagen are implicitly considered through effective parameters of the model. Additionally, one should in principle also consider the translational free energy of the filament components, which is larger for filaments wetting ERES than for free filaments. However, this contribution is relatively minor compared to the rest of contributions to the free energy and hence we disregard it in our formal analysis of the system free energy.

In total, the extensive free energy of the system, F, is the addition of the different free energy terms in ***Equations (M1–M4)***,

$$F = F_{bend} + F_{line} + F_{pol} + F_{phen}. \qquad \textbf{(M5)}$$

Disregarding the constant term coming from the polymerization free energy, F_{pol}, we end up getting the expression shown in the main text ***Equation (1)***.

DETAILED DESCRIPTION OF THE PHYSICAL MODEL OF TANGO1-DEPENDENT TRANSPORT INTERMEDIATE FORMATION

Here we present the detailed description and derivation, as well as the mathematical formalism of the analysis of the physical model of TANGO1-dependent transport intermediate formation presented in the main text. Our model builds on a previously presented mechanical model for clathrin-coated vesicle formation (Saleem *et al.*, 2015), which we extended to allow for the growth of larger transport intermediates by incorporating *(i)* the effects of TANGO1 rings on COPII coats; *(ii)* the reduction of the membrane tension by the tethering and fusion of ERGIC53-containing membranes; and *(iii)* an outward-directed force (***Figure S3A***).

Analogously to the clathrin vesicle model by Saleem et al. (Saleem *et al.*, 2015), we consider that the free energy per unit area of coat polymerization onto the membrane, μ_c, has a bipartite contribution arising from the positive free energy of COPII binding to the membrane, ${\mu_c}^0$, and from the negative contribution of membrane deformation by bending, so $\mu_c = {\mu_c}^0 - 2\frac{\kappa_b}{R^2}$, where κ_b is the bending rigidity of the lipid bilayer, and R is the radius of curvature imposed by the polymerized COPII coat. An additional term associated to the possible elastic deformation of the COPII coat could be considered as $\mu_{coat,bend} = -\frac{1}{2}\kappa_{coat}\left(\frac{2}{R} - \frac{2}{R_{coat}}\right)^2$, where κ_{coat} is the coat rigidity and R_{coat} is the spontaneous radius of curvature of the coat (Iglič, Slivnik and Kralj-Iglič, 2007; Boucrot *et al.*, 2012). However, we assume that the coat is considerably more rigid than the membrane, $\kappa_{coat} \gg \kappa_b$, so there is no coat deformation and $R = R_{coat}$. Hence, the free energy per unit area of the initially undeformed membrane due to COPII polymerization, f_{coat}, can be expressed as

$$f_{coat} = \frac{-\mu_c A_c}{A_p}, \qquad \textbf{(M6)}$$

where A_c is the surface area of the membrane covered by the COPII coat, and A_p is the projected area of the carrier, that is, the area of the initially undeformed membrane under the carrier (***Figure S3B***). In contrast to our previous analysis of the two-dimensional scenario of TANGO1 ring formation, here we consider the bending of the membrane away from the initially flat structure, and so we do not consider the phenomenological term of ERES size, ***Equation (M4)***, but rather the free energy associated to coat polymerization, ***Equation (M6)***.

We also consider a line energy for the coat subunits laying at the edge of the polymerizing structure. This line energy per unit area reads as

$$f_{line} = \lambda(\omega)\frac{l}{A_p}, \qquad \textbf{(M7)}$$

where $\lambda(\omega) = \lambda_0 - \omega\,\Delta\lambda$ is the line tension, consisting on the line tension of the bare coat, λ_0, and $\Delta\lambda$ is the line tension reduction associated with the TANGO1-filement wetting; and $l = 2\pi\rho$ is the length of the carrier edge, associated to the opening radius at the base of the carrier, ρ (***Figure S3B***).

Next, we consider the effect of the membrane tension. We consider that the membrane is initially under a certain tension, σ_0, and it can get a local decrease in tension, $\Delta\sigma$, by the fusion of

incoming ERGIC53-containing membranes. Hence, the actual membrane tension at a given moment is $\sigma = \sigma_0 - \Delta\sigma$. We can estimate that $\Delta\sigma = K_s\, m\, A_{ERGIC}$, where K_s is the stretching coefficient of the membrane, and A_{ERGIC} is the surface area of each of the m ERGIC53-containing vesicles that fuse to the budding site (Sens and Turner, 2006). Hence, the tension associated free energy per unit area reads,

$$f_{tension} = (\sigma_0 - \Delta\sigma)\frac{A_m}{A_p}, \qquad \textbf{(M8)}$$

where A_m is the surface area of the entire membrane after deformation.

Next, we consider the contribution of the TANGO1 filament into the free energy of the system. Analogously to our discussion for the free energy of coat binding to the membrane, ***Equation (M6)***, we can write this free energy per unit area as

$$f_T = -\frac{\mu_T\, l_T}{A_p}, \qquad \textbf{(M9)}$$

where $\mu_T = {\mu_T}^0 - \frac{\kappa_T}{2}\left(\frac{1}{R_T} - {c_0}^T\right)^2$ includes the contributions of the filament assembly energy, ${\mu_T}^0$, and of the filament bending energy as explained in the ring formation model, where κ_T is the filament bending rigidity, R_T is the ring radius, and ${c_0}^T$ is the preferred filament curvature. Under conditions of full wetting of the TANGO1 filament, the size of the ring radius equals to the size of the coat opening, that is $R_T = \rho$. We want to stress that the bending energy penalty of the filament diverges when the bud approaches closure, meaning that either there is partial dewetting of the TANGO1 filament from the edge of the COPII coat at narrow necks or the shape transition of the carrier goes through intermediate shapes with a relatively large bud neck, such as Delaunay shapes (e.g. unduloids) (Naito and Ou-Yang, 1997).

Finally, the mechanical work performed by the outward-directed force, N, is also included in the free energy of the system, as

$$f_f = -\frac{N\, h}{A_p}, \qquad \textbf{(M10)}$$

where h is the length of the carrier (***Figure S3B***). At this stage, we disregard the effects of the growth-shrinkage dynamics of the polymerizing COPII lattice, as included in our formal analysis of TANGO1 ring size through the phenomenological term in the free energy, ***Equation (M4)***. Hence, the total free energy of the carrier per unit area, f_c, is the sum of all these contributions ***Equations (M6-10)***,

$$f_c = f_{coat} + f_{line} + f_{tension} + f_T + f_f, \qquad \textbf{(M11)}$$

which is presented in ***Equation (5)*** in the main text.

Geometry of the problem

Based on the proposed geometries for the growing carrier we can distinguish three geometries, depending on how complete the transport intermediate is: shallow buds, deep buds, and pearled

intermediates (***Figure S3B***, panels *(i)* to *(iii)*, respectively). These shapes will allow us to calculate as a function of the carrier morphology the geometric parameters that enter in ***Equation (5)***, namely, the area of the coat, A_c, the area of the membrane, A_m, the projected area, A_p, and the length of the coat rim, l (Saleem *et al.*, 2015). A convenient quantity to parametrize the shape of the carrier is the height of the carrier, h, which we will use in a dimensionless manner by normalizing it to the diameter of the spherical bud, $\eta = h/2R$.

(i) Shallow bud. For a shallow bud (***Figure S4B(i)***), which corresponds to buds smaller than a hemisphere, we can write that $A_c = A_m = 2\pi R^2\,(1-\cos\theta)$, where $0 < \theta < \pi/2$ is the opening angle of the bud (see ***Figure S3B(i)***). In addition, $A_p = \pi\rho^2 = \pi R^2 \sin^2\theta$; and $h = R(1-\cos\theta)$. Expressing these quantities as a function of the shape parameter, η, we obtain

$$A_c = A_m = 4\pi R^2\eta : \eta < \tfrac{1}{2}, \quad \textbf{(M12)}$$

$$A_p = 4\pi R^2\eta\,(1-\eta) : \eta < \tfrac{1}{2}, \quad \textbf{(M13)}$$

$$\rho = 2R\sqrt{\eta(1-\eta)} : \eta < \tfrac{1}{2}. \quad \textbf{(M14)}$$

(ii) Deep bud. For a deep bud (***Figure S3B(ii)***), which corresponds to buds larger than a hemisphere, we can write that $A_c = 2\pi R^2\,(1-\cos\theta)$, where $\pi/2 < \theta < \pi$. In addition, $A_m = \pi R^2\,(1+(1-\cos\theta)^2)$; $A_p = \pi R^2$; and $h = R(1-\cos\theta)$. Expressing these quantities as a function of the shape parameter, η, which in this case ranges between ½<$\eta < 1$, we obtain

$$A_c = 4\pi R^2\eta : \tfrac{1}{2} < \eta < 1\,, \quad \textbf{(M15)}$$

$$A_m = \pi R^2(1+4\eta^2) : \tfrac{1}{2} < \eta < 1\,, \quad \textbf{(M16)}$$

$$A_p = \pi R^2 : \tfrac{1}{2} < \eta < 1\,, \quad \textbf{(M17)}$$

$$\rho = 2R\sqrt{\eta(1-\eta)} : \tfrac{1}{2} < \eta < 1\,. \quad \textbf{(M18)}$$

(iii) Pearled intermediate. A pearled intermediate corresponds to carriers form by an incomplete bud with opening angle $0 < \theta < \pi$, connected via a narrow connection with n complete buds (***Figure S3B(iii)***). Here, we can write that $A_c = 2\pi R^2\,[2n + (1-\cos\theta)]$, where $0 < \theta < \pi$ and $n \geq 1$. In addition, $A_m = \pi R^2\,[4n + 1 + (1-\cos\theta)^2]$; $A_p = \pi R^2$; and $h = R(2n+1-\cos\theta)$. Expressing these quantities as a function of the shape parameter, η, we obtain

$$A_c = 4\pi R^2\eta : \eta > 1\,, \quad \textbf{(M19)}$$

$$A_m = \pi R^2(1+4n+4(\eta-n)^2) : \eta > 1\,, \quad \textbf{(M20)}$$

$$A_p = \pi R^2 : \eta > 1\,, \quad \textbf{(M21)}$$

$$\rho = 2R\sqrt{(\eta-n)-(\eta-n)^2} : \eta > 1\,. \quad \textbf{(M22)}$$

Putting together ***Equations (M12-22)***, we get:

$$A_c = 4\pi R^2\eta \quad \textbf{(M23)}$$

$$A_m = \begin{cases} 4\pi R^2\eta, & \eta < 1/2 \\ \pi R^2[1+4n+4(\eta-n)^2], & \eta > 1/2 \end{cases} \quad \textbf{(M24)}$$

$$A_p = \begin{cases} 4\pi R^2 \eta(1-\eta), & \eta < 1/2 \\ \pi R^2, & \eta > 1/2 \end{cases} \quad \textbf{(M25)}$$

$$\rho = 2R\sqrt{(\eta - n) - (\eta - n)^2}\,. \quad \textbf{(M26)}$$

where $n = [\eta]$, the brackets denoting the integer part operator. This allows us to express ***Equation (5)***, for the case where $c_0 = 0$ and under full wetting conditions ($\omega = 1$), as

$$f_c = \frac{\sigma - \tilde{\mu}}{1-\eta} + \frac{\tilde{\lambda}}{\sqrt{\eta(1-\eta)}} + \frac{\tilde{\kappa}_T}{[\eta(1-\eta)]^{3/2}}, \qquad \eta < 1/2 \quad \textbf{(M27)}$$

$$f_c = \sigma[1 + 4n + 4(\eta - n)^2] - 4\tilde{\mu}\eta + 4\tilde{\lambda}\sqrt{(\eta - n)(1 - \eta + n)} + \frac{4\tilde{\kappa}_T}{\sqrt{(\eta-n)(1-\eta+n)}}, \qquad \eta > 1/2, \quad \textbf{(M28)}$$

where $\tilde{\mu} = {\mu_c}^0 - 2\frac{\kappa_b}{R^2} + \frac{N}{2\pi R}$, $\tilde{\lambda} = (\lambda_0 - \Delta\lambda - {\mu_T}^0)/R$, and $\tilde{\kappa}_T = \kappa_T/8R^3$.

ACKNOWLEDGEMENTS

We thank Javier Diego Íñiguez and members of the Garcia-Parajo lab for valuable discussions. M.F. Garcia-Parajo and V. Malhotra are Institució Catalana de Recerca i Estudis Avançats professors at ICFO-Institut de Ciencies Fotoniques and the Centre for Genomic Regulation (CRG), respectively. M.F. Garcia-Parajo and F. Campelo acknowledge support by the Spanish Ministry of Economy and Competitiveness ("Severo Ochoa" Programme for Centres of Excellence in R&D (SEV-2015-0522), BFU2015-73288-JIN, FIS2015-63550-R and FIS2017-89560-R), Fundacion Privada Cellex, Generalitat de Catalunya through the CERCA program, ERC Advanced Grant NANO-MEMEC (GA 788546) and LaserLab 4 Europe (GA 654148). I. Raote and V. Malhotra acknowledge funding by grants from the Ministerio de Economía, Industria y Competitividad Plan Nacional (BFU2013-44188-P) and Consolider (CSD2009-00016); support of the Spanish Ministry of Economy and Competitiveness, through the Programmes "Centro de Excelencia Severo Ochoa 2013–2017" (SEV-2012–0208) and Maria de Maeztu Units of Excellence in R and D (MDM-2015–0502); and support of the CERCA Programme/Generalitat de Catalunya. All the authors acknowledge support by the BIST Ignite Grant (eTANGO). I. Raote acknowledges support from the Spanish Ministry of Science, Innovation and Universities (IJCI-2017-34751). This work reflects only the authors' views, and the EU Community is not liable for any use that may be made of the information contained therein.

1004 **TABLE 1: Parameters used in the large transport intermediate formation model.** The free
1005 energy ***Equation (5)*** depends on a number of different elastic and geometric parameters, which
1006 are described in this table.

Parameter	Description	Value	Notes	Reference
σ_0	ER membrane tension	$0.003\ k_BT/nm^2$		(Upadhyaya and Sheetz, 2004)
K_s	Stretching modulus of the membrane	$10^{-8}\ k_BT/nm^4$		(Sens and Turner, 2006)
m	Number of fused vesicles	0–4		(Raote *et al.*, 2018)
A_{ERGIC}	Membrane area of the fused vesicle	$10^3\ nm^2$	Membrane area of an average COPI vesicle	(Bykov *et al.*, 2017)
λ_0	Bare coat line tension	$0.012\ k_BT/nm$	Not measured for COPII. Used the clathrin value as a reference	(Saleem *et al.*, 2015)
$\Delta\lambda$	Linactant TANGO1 effect	Unknown (varies from 0 to λ_0)		-
${\mu_c}^0$	COPII coat binding energy	Variable. The measured value for clathrin is $0.024\ k_BT/nm^2$		(Saleem *et al.*, 2015)
κ_b	Membrane bending rigidity	$20\ k_BT$		(Niggemann, Kummrow and Helfrich, 1995)
${\mu_T}^0$	TANGO1 filament lateral binding energy	$0.15–1\ k_BT/nm$	Not measured. Range based on standard protein-protein interaction energies ($5–30\ k_BT$)	
κ_T	TANGO1 filament bending rigidity	$120\ k_BT\ nm$	Not measured. Range based on standard filament rigidities (see text)	
${c_0}^T$	TANGO1 filament spontaneous curvature	$(-0.01,0.01)\ nm^{-1}$	Not measured.	
N	Outwards directed force	$0-5\ pN$	Not measured. Range based	(Kovar and Pollard, 2004) (Actin); (Block

			on known intracellular forces.	*et al.*, 2003) (Molecular motors)
R	Radius of curvature of the COPII coat	37.5 nm		(Miller and Schekman, 2013)
R_T	Radius of stationary TANGO1 ring	100 nm		(Raote *et al.*, 2017)

1007

APPENDIX 1. Computation of the free energy transitions promoting ring-ring fusion

In the main body of this article, we have considered the situation where TANGO1 filaments form circular rings around ERES. However, we previously reported situations where TANGO1 filaments form other structures rather than circular rings, such as linear or planar arrangements of similarly fused rings (Raote *et al.*, 2018). Hence, we decided to exploit our model to compute the ability of nearby TANGO1 rings to form fused structures and propose a ring fusion pathway consisting on transient filament breakage, partial dewetting, merger to a neighboring filament, and final rewetting (***Appendix 1–Figure 1***, ***Figure S4A***). Each of these transitions is characterized by a free energy change (***Appendix 1–Figure 1B***, ***Figure S4B-G***).

To compute the free energy changes leading to ring fusion, we consider, for simplicity, two closely apposed TANGO1 rings, separated from each other by a center-to-center distance a (see ***Figure S1A***). We start by analyzing the partial dewetting of the TANGO1 ring due to transient breakage of the TANGO1 filament and partial detachment of a region of the filament (given by an angle α) from the COPII patch (***Appendix 1–Figure 1A*** and ***Figure S4A***), by computing the free energy changes of the shape transition. The energy change upon partial dewetting of the TANGO1 filament depends on different factors, namely the strength of TANGO1-COPII interaction (that is, on $\overline{\Delta\lambda}$), which prevents dewetting; the bending rigidity, κ_T, and spontaneous curvature, c_0, of the filament, which generally favor partial dewetting; and the free energy of generating new loose filament ends, ε_{free}, which prevents dewetting by penalizing filament breakage. Let us now calculate these changes according to our model. In the following, we consider only two neighboring ERES of a fixed size, R, and compute the energy changes per ERES, as depicted schematically in ***Appendix 1–Figure 1B***.

First, opening of the filament, by the transient, stochastic breakage of a link between two components of the TANGO1 filament, is associated with a free energy change $\Delta F_{break} = 2\varepsilon_{free}$.

Second, the free energy of partial dewetting is given then by the expression

$$\Delta F_{dewet}(\alpha) = 2R\alpha[\Delta\lambda - \kappa_T/2(1/R - c_0)^2] + 2\varepsilon_{free}, \qquad \textbf{(A1)}$$

where we considered that the portion of the filament that detached from the COPII patch rapidly adopts the preferred curvature, c_0. Since $\varepsilon_{free} \geq 0$, such a partial dewetting transition is energetically unfavorable under the conditions of total wetting of the filament and hence only occurs stochastically with a probability proportional to $e^{-\Delta F_{dewett}(\alpha)/k_B T}$, following Arrhenius kinetics.

If there are free TANGO1 monomers or another partially dewetted TANGO1 ring nearby, the loose end of one partially dewetted filament can bind the nearby partially dewetted TANGO1 filament. This transition is characterized by an overall free energy change, $\Delta F_{fusion}(\alpha)$, which depends on the actual shape of the interconnecting piece of filament between the two rings. To obtain an analytically treatable expression for the free energy change upon fusion, we approximate the shape of this interconnecting filament as a circular line matching the filament ring piece wetting the COPII patch (see ***Figure S4A***, subpanel (4)). Geometric arguments imply that

the radius of curvature of this interconnecting piece of filament is given by $R_{int}(\alpha) = 1/(2\cos\alpha) - R$, and the distance to the symmetry axis (see ***Figure S4A***, subpanel (4)) by $\Delta = a/2\,(\tan\alpha - 1/\cos\alpha) + R$. If we ignore filament growth during the partial dewetting situation, we can see that fusion is only possible if the two rings are at a distance below a maximal fusion distance $a_{max}(\alpha) = 2\alpha R$. Moreover, the condition $\Delta \geq 0$ leads to a minimum dewetting angle allowing partial ring fusion, given by $\alpha_{min}(a) = \arcsin\left(\frac{1-4R^2/a^2}{1+4R^2/a^2}\right)$. In the fused configuration, we search for the partial dewetting angle, $\alpha_{min} \leq \alpha_{fusion} \leq \pi/2$, that minimizes the overall free energy change in the system after ring fusion, calculated with respect to the initial total wetting situation,

$$\Delta F_{fusion}(\alpha) = 2R\alpha(\Delta\lambda + \kappa_T/2[(1/R_{int}(\alpha) + c_0)^2 - (1/R - c_0)^2]) + 2\varepsilon_{free}, \quad \textbf{(A2)}$$

which is again positive if we assume the system is in the wetting regime, that is, $\Delta\lambda \geq \kappa_T/2(1/R - c_0)^2$ (see ***Figure S4B***). However, the free energy change from the partially dewetted, pre-fusion state intermediate (subpanel (4), ***Figure S4A***) to the fused ring situation is given by $-\Delta F_{break} = -2\varepsilon_{free}$, which takes negative values and therefore leads to the fused ring geometry to be a metastable configuration. Hence, the stochastic breakage of a link in the TANGO1 filament followed by partial dewetting could, under certain circumstances, be resolved by the fusion of this open TANGO1 filament with another open TANGO1 filament nearby, thus generating a fused ring configuration.

Finally, since the system is under wetting conditions, once the two filaments have merged, the COPII patches will also tend to fuse and be completely wet by the fused TANGO1 filament (see subpanel (6) in ***Appendix 1–Figure 1***). This would normally be a spontaneous process associated with the decrease in the ERES free energy. To have an estimate of this effect, we consider a simple geometry for the fused rings, schematized in ***Figure S4A***, subpanel (6), as that of two connecting circular segments. Since we rarely observed experimentally intermediate states (Raote *et al.*, 2018), we assume that the dynamics of merger and rewetting events is relatively fast so we consider that there is no filament growth during this time. Hence, the filament length in the fused situation is just twice the length of a single wetting filament, and also that restructuring is fast enough to not let the COPII patch grow, so the membrane area covered by COPII subunits in the fused ring configuration is twice the area covered by a pre-fused single ERES. With these two conditions, and the geometry schematized in ***Figure S4C***, we can write down the expression for the free energy change per ERES with respect to the initial situation as

$$\Delta F_{spread}(\beta) = \kappa_T\left[\left(\frac{1}{R_1} - c_0\right)^2(\pi - \beta)R_1 + \left(\frac{1}{R_2} + c_0\right)^2(\pi R - (\pi - \beta)R_1) - \left(\frac{1}{R} - c_0\right)^2\pi R\right], \quad \textbf{(A3)}$$

where $R_2 = 2(R - (1 - \beta/\pi)R_1)/(1 - 2\beta/\pi)$, and R_1 is given by the solution of the quartic equation,

$$3R^2 - 4RR_1 + {R_1}^2 - \frac{(2R^2 - 4RR_1 + {R_1}^2)\beta}{\pi} + (R_1 - 2R)\sqrt{\frac{(R_1 - 2R)^2\cos^2\beta}{(\pi - 2\beta)^2}}\sin\beta = 0. \quad \textbf{(A4)}$$

The angle β is then optimized as that corresponding to the minimal energy of the fused ring configuration with respect to the isolated ring configuration (***Figure S4D***).

We computed the energy barrier required to be overcome to allow ring fusion, ΔF_{fusion} (***Appendix 1–Figure 1C***). Our results indicate that a decrease in the interaction energy between TANGO1 filaments and COPII subunits leads to lower fusion energy barriers (***Appendix 1–Figure 1C***) and hence more efficient ring fusion, as experimentally observed (Raote *et al.*, 2018). We also computed whether the overall fusion process is energetically favorable or not, which indicates whether the fused configuration can be even formed *de novo* before circular rings are fully assembled, indicating that negative filament spontaneous curvatures promote the stabilization of the fused ring configuration since they stabilize association of the concave face of the filament with COPII subunits (***Figure S4G***). Altogether, the results of our theoretical model show that the closer the system is to the wetting-dewetting transition, the more feasible it is to observe spontaneous formation of fused TANGO1 rings (***Appendix 1–Figure 1D***). These results agree with the experimental observation that in cells expressing the mutant of TANGO1 that is unable to bind COPII subunits (TANGO1-ΔPRD mutant), TANGO1 appears as a set of linearly or planarly fused rings (Raote *et al.*, 2018).

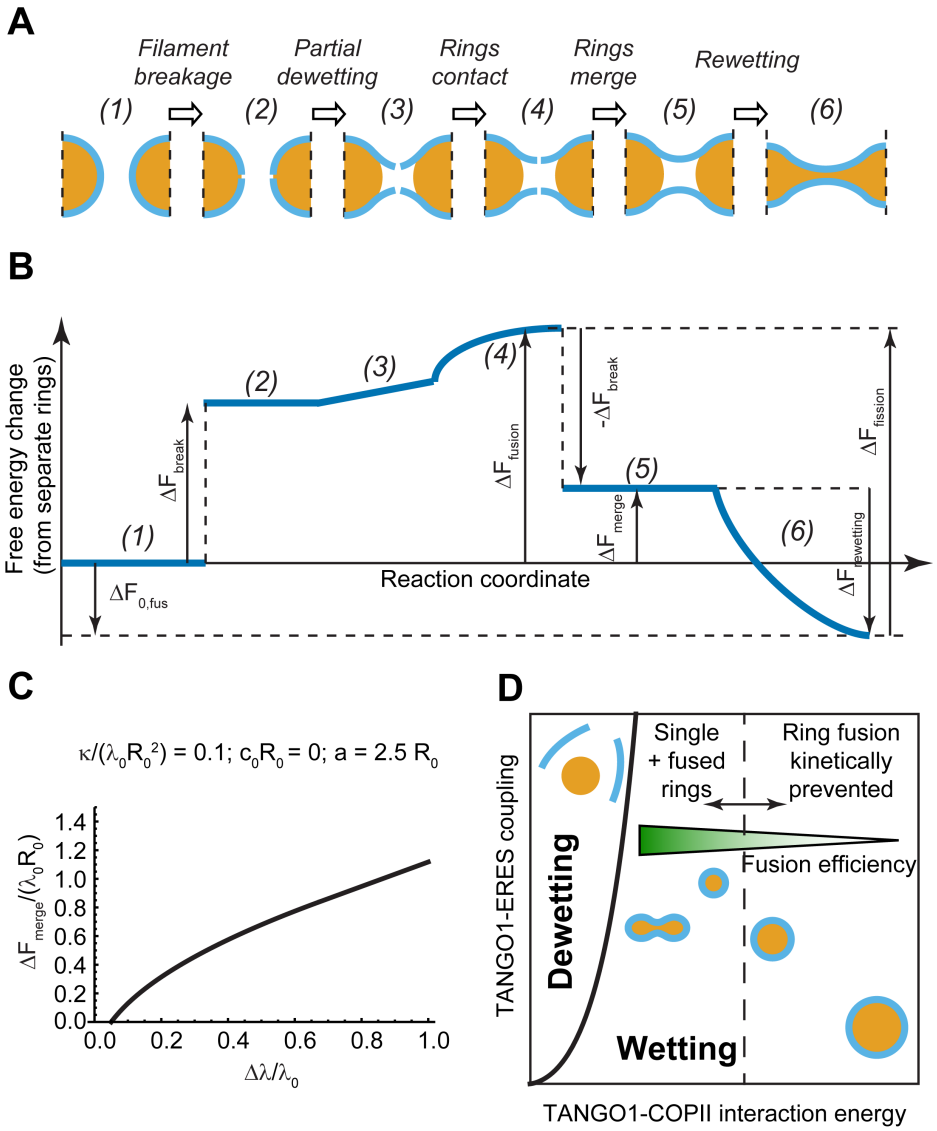

Appendix 1 – Figure 1. Formation of fused TANGO1 rings.

(A) Schematic representation of the pathway leading to fusion of nearby ERES wetted by TANGO1 filaments (see text for details). **(B)** Schematic representation of the free energy transitions paralleling the ring fusion pathway in panel **(A)** (see text for details). **(C)** Ring merger energy (that is, the barrier for ring fusion minus the filament breaking energy) as a function of the linactant strength of TANGO1, $\overline{\Delta\lambda}$, for rings separated by a distance $a = 2.5\,R_0$, a dimensionless bending rigidity of the filament $\overline{\kappa_T} = 0.1$ and a vanishing spontaneous curvature. **(D)** Summary of the model's results, indicating the wetting-dewetting transition as in Figure 2A. Cartoons of the expected structures are shown as well as the efficiency of ring fusion. Qualitatively, for values larger than some cutoff value of the TANGO1-COPII interaction energy, which is linked to $\overline{\Delta\lambda}$, the energy barrier for ring fusion is too large and ring fusion is kinetically prevented.

REFERENCES

Apodaca, G. (2002) 'Modulation of membrane traffic by mechanical stimuli', *American Journal of Physiology-Renal Physiology*. American Physiological SocietyBethesda, MD , 282(2), pp. F179–F190. doi: 10.1152/ajprenal.2002.282.2.F179.

Aridor, M. (2018) 'COPII gets in shape: Lessons derived from morphological aspects of early secretion.', *Traffic (Copenhagen, Denmark)*, 19(11), pp. 823–839. doi: 10.1111/tra.12603.

Bard, F. *et al.* (2006) 'Functional genomics reveals genes involved in protein secretion and Golgi organization.', *Nature*, 439(February), pp. 604–607. doi: 10.1038/nature04377.

Beck, M. and Baumeister, W. (2016) 'Cryo-Electron Tomography: Can it Reveal the Molecular Sociology of Cells in Atomic Detail?', *Trends in Cell Biology*, 26(11), pp. 825–837. doi: 10.1016/j.tcb.2016.08.006.

Bevis, B. J. *et al.* (2002) 'De novo formation of transitional ER sites and Golgi structures in Pichia pastoris.', *Nature cell biology*, 4(10), pp. 750–6. doi: 10.1038/ncb852.

Block, S. M. *et al.* (2003) 'Probing the kinesin reaction cycle with a 2D optical force clamp.', *Proceedings of the National Academy of Sciences of the United States of America*, 100(5), pp. 2351–6. doi: 10.1073/pnas.0436709100.

Bottanelli, F. *et al.* (2016) 'Two-colour live-cell nanoscale imaging of intracellular targets', *Nature Communications*. Nature Publishing Group, 7(1), p. 10778. doi: 10.1038/ncomms10778.

Boucrot, E. *et al.* (2012) 'Membrane fission is promoted by insertion of amphipathic helices and is restricted by crescent BAR domains', *Cell*. 2012/04/03, 149(1), pp. 124–136. doi: 10.1016/j.cell.2012.01.047.

Bykov, Y. S. *et al.* (2017) 'The structure of the COPI coat determined within the cell', *eLife*, 6. doi: 10.7554/eLife.32493.

Campelo, F. *et al.* (2017) 'Sphingomyelin metabolism controls the shape and function of the golgi cisternae', *eLife*, 6. doi: 10.7554/eLife.24603.

Derényi, I., Jülicher, F. and Prost, J. (2002) 'Formation and interaction of membrane tubes.', *Physical review letters*, 88(23), p. 238101. doi: 10.1103/PhysRevLett.88.238101.

Doi, M. (Masao) and Edwards, S. F. (Sam F. (1986) *The theory of polymer dynamics*. Clarendon Press.

Faini, M. *et al.* (2013) 'Vesicle coats: structure, function, and general principles of assembly.', *Trends in cell biology*, 23(6), pp. 279–88. doi: 10.1016/j.tcb.2013.01.005.

Farhan, H. *et al.* (2008) 'Adaptation of endoplasmic reticulum exit sites to acute and chronic increases in cargo load.', *The EMBO journal*, 27(15), pp. 2043–54. doi: 10.1038/emboj.2008.136.

Fletcher, D. A. and Mullins, R. D. (2010) 'Cell mechanics and the cytoskeleton.', *Nature*, 463(7280), pp. 485–92. doi: 10.1038/nature08908.

Foret, L. (2005) 'A simple mechanism of raft formation in two-component fluid membranes', *Europhysics Letters (EPL)*. IOP Publishing, 71(3), pp. 508–514. doi: 10.1209/epl/i2005-10098-x.

Forster, R. *et al.* (2006) 'Secretory Cargo Regulates the Turnover of COPII Subunits at Single ER Exit Sites', *Current Biology*, 16(2), pp. 173–179. doi: 10.1016/j.cub.2005.11.076.

Frolov, V. A. J. *et al.* (2006) '"Entropic Traps" in the Kinetics of Phase Separation in Multicomponent Membranes Stabilize Nanodomains', *Biophysical Journal*, 91(1), pp. 189–205. doi: 10.1529/biophysj.105.068502.

1176 Glick, B. S. (2017) *New insights into protein secretion: TANGO1 runs rings around the COP*
1177 *II coat*, *Journal of Cell Biology*. doi: 10.1083/jcb.201701142.

1178 Gorur, A. *et al.* (2017) 'COPII-coated membranes function as transport carriers of
1179 intracellular procollagen I', 216(6), pp. 1745–1759. doi: 10.1083/jcb.201702135.

1180 Hammond, A. T. and Glick, B. S. (2000) 'Dynamics of Transitional Endoplasmic Reticulum
1181 Sites in Vertebrate Cells', *Molecular Biology of the Cell*. Edited by H. R. B. Pelham, 11(9),
1182 pp. 3013–3030. doi: 10.1091/mbc.11.9.3013.

1183 Hassinger, J. E. *et al.* (2017) 'Design principles for robust vesiculation in clathrin-mediated
1184 endocytosis.', *Proceedings of the National Academy of Sciences of the United States of*
1185 *America*. National Academy of Sciences, 114(7), pp. E1118–E1127. doi:
1186 10.1073/pnas.1617705114.

1187 Heinzer, S. *et al.* (2008) 'A model for the self-organization of exit sites in the endoplasmic
1188 reticulum.', *Journal of cell science*, 121(Pt 1), pp. 55–64. doi: 10.1242/jcs.013383.

1189 Hughes, H. *et al.* (2009) 'Organisation of human ER-exit sites: requirements for the
1190 localisation of Sec16 to transitional ER.', *Journal of cell science*, 122(Pt 16), pp. 2924–34.
1191 doi: 10.1242/jcs.044032.

1192 Hutchings, J. *et al.* (2018) 'Subtomogram averaging of COPII assemblies reveals how coat
1193 organization dictates membrane shape', *Nature Communications*, 9(1), p. 4154. doi:
1194 10.1038/s41467-018-06577-4.

1195 Iglič, A., Slivnik, T. and Kralj-Iglič, V. (2007) 'Elastic properties of biological membranes
1196 influenced by attached proteins', *Journal of Biomechanics*, 40(11), pp. 2492–2500. doi:
1197 10.1016/j.jbiomech.2006.11.005.

1198 Ishikawa, Y. *et al.* (2016) 'Intracellular mechanisms of molecular recognition and sorting for
1199 transport of large extracellular matrix molecules', *Proceedings of the National Academy of*
1200 *Sciences*. doi: 10.1073/pnas.1609571113.

1201 Ito, Y., Uemura, T. and Nakano, A. (2018) 'The Golgi entry core compartment functions as a
1202 COPII-independent scaffold for ER-to-Golgi transport in plant cells', *J Cell Sci*. The
1203 Company of Biologists Ltd, 131(2), p. jcs203893. doi: 10.1242/JCS.203893.

1204 Kadler, K. E. *et al.* (2007) 'Collagens at a glance', *Journal of Cell Science*, 120(12).

1205 Kosmalska, A. J. *et al.* (2015) 'Physical principles of membrane remodelling during cell
1206 mechanoadaptation', *Nature Communications*. Nature Publishing Group, 6(1), p. 7292. doi:
1207 10.1038/ncomms8292.

1208 Koster, G. *et al.* (2003) 'Membrane tube formation from giant vesicles by dynamic
1209 association of motor proteins', *Proceedings of the National Academy of Sciences*, 100(26),
1210 pp. 15583–15588. doi: 10.1073/pnas.2531786100.

1211 Kovar, D. R. and Pollard, T. D. (2004) 'Insertional assembly of actin filament barbed ends in
1212 association with formins produces piconewton forces.', *Proceedings of the National Academy*
1213 *of Sciences of the United States of America*, 101(41), pp. 14725–30. doi:
1214 10.1073/pnas.0405902101.

1215 Kozlov, M. M. *et al.* (2014) 'Mechanisms shaping cell membranes', *Current Opinion in Cell*
1216 *Biology*, 29(1). doi: 10.1016/j.ceb.2014.03.006.

1217 Leduc, C. *et al.* (2004) 'Cooperative extraction of membrane nanotubes by molecular
1218 motors', *Proceedings of the National Academy of Sciences*, 101(49), pp. 17096–17101. doi:
1219 10.1073/pnas.0406598101.

1220 Lee, S.-H. *et al.* (2012) 'Counting single photoactivatable fluorescent molecules by
1221 photoactivated localization microscopy (PALM)', *Proceedings of the National Academy of*
1222 *Sciences*, 109(43), pp. 17436–17441. doi: 10.1073/pnas.1215175109.

1223 Liu, M. *et al.* (2017) 'Tango1 spatially organizes ER exit sites to control ER export', *Journal*
1224 *of Cell Biology*. doi: 10.1083/jcb.201611088.

1225 Liu, T.-L. *et al.* (2018) 'Observing the cell in its native state: Imaging subcellular dynamics in
1226 multicellular organisms.', *Science (New York, N.Y.)*. American Association for the
1227 Advancement of Science, 360(6386), p. eaaq1392. doi: 10.1126/science.aaq1392.

1228 Luxton, G. W. G. *et al.* (2010) 'Linear arrays of nuclear envelope proteins harness retrograde
1229 actin flow for nuclear movement.', *Science (New York, N.Y.)*, 329(5994), pp. 956–9. doi:
1230 10.1126/science.1189072.

1231 Ma, W. and Goldberg, J. (2016) 'TANGO1/cTAGE5 receptor as a polyvalent template for
1232 assembly of large COPII coats', *Proceedings of the National Academy of Sciences*. doi:
1233 10.1073/pnas.1605916113.

1234 Maeda, M., Katada, T. and Saito, K. (2017) 'TANGO1 recruits Sec16 to coordinately
1235 organize ER exit sites for efficient secretion', *The Journal of Cell Biology*, 216(6), pp. 1731–
1236 1743. doi: 10.1083/jcb.201703084.

1237 Maeda, M., Saito, K. and Katada, T. (2016) 'Distinct isoform-specific complexes of
1238 TANGO1 cooperatively facilitate collagen secretion from the endoplasmic reticulum',
1239 *Molecular Biology of the Cell*. doi: 10.1091/mbc.E16-03-0196.

1240 McCaughey, J. *et al.* (2019) 'ER-to-Golgi trafficking of procollagen in the absence of large
1241 carriers', *The Journal of Cell Biology*, 218(3), pp. 929–948. doi: 10.1083/jcb.201806035.

1242 Miller, E. A. and Schekman, R. (2013) 'COPII - a flexible vesicle formation system.',
1243 *Current opinion in cell biology*, 25(4), pp. 420–7. doi: 10.1016/j.ceb.2013.04.005.

1244 Mironov, A. A. *et al.* (2003) 'ER-to-Golgi carriers arise through direct en bloc protrusion and
1245 multistage maturation of specialized ER exit domains.', *Developmental cell*. Elsevier, 5(4),
1246 pp. 583–94. doi: 10.1016/S1534-5807(03)00294-6.

1247 Mouw, J. K., Ou, G. and Weaver, V. M. (2014) 'Extracellular matrix assembly: a multiscale
1248 deconstruction', *Nature Reviews Molecular Cell Biology*, 15(12), pp. 771–785. doi:
1249 10.1038/nrm3902.

1250 Naito, H. and Ou-Yang, Z. (1997) 'Analytical solutions to Helfrich variation problem for
1251 shapes of lipid bilayer vesicles'. 物性研究刊行会.

1252 Niggemann, G., Kummrow, M. and Helfrich, W. (1995) 'The bending rigidity of
1253 phosphatidylcholine bilayers: dependences on experimental method, sample cell sealing and
1254 temperature', *Journal de Physique II*. EDP Sciences, 5(3), pp. 413–425. doi:
1255 10.1051/jp2:1995141.

1256 Nixon-Abell, J. *et al.* (2016) 'Increased spatiotemporal resolution reveals highly dynamic
1257 dense tubular matrices in the peripheral ER', *Science*, 354(6311).

1258 Nogueira, C. *et al.* (2014) 'SLY1 and syntaxin 18 specify a distinct pathway for procollagen
1259 VII export from the endoplasmic reticulum', *eLife*. doi: 10.7554/eLife.02784.

1260 Omari, S. *et al.* (2018) 'Noncanonical autophagy at ER exit sites regulates procollagen
1261 turnover.', *Proceedings of the National Academy of Sciences of the United States of America*.
1262 National Academy of Sciences, 115(43), pp. E10099–E10108. doi:
1263 10.1073/pnas.1814552115.

1264 Pinot, M., Goud, B. and Manneville, J.-B. (2010) 'Physical aspects of COPI vesicle
1265 formation.', *Molecular membrane biology*, 27(8), pp. 428–42. doi:
1266 10.3109/09687688.2010.510485.

1267 Raote, I. *et al.* (2017) 'TANGO1 assembles into rings around COPII coats at ER exit sites.',
1268 *The Journal of cell biology*. Rockefeller University Press, 216(4), pp. 901–909. doi:
1269 10.1083/jcb.201608080.

1270 Raote, I. *et al.* (2018) 'TANGO1 builds a machine for collagen export by recruiting and
1271 spatially organizing COPII, tethers and membranes', *eLife*, 7. doi: 10.7554/eLife.32723.

1272 Raote, I. and Malhotra, V. (2019) 'Protein transport by vesicles and tunnels.', *The Journal of*
1273 *cell biology*. Rockefeller University Press, p. jcb.201811073. doi: 10.1083/jcb.201811073.

1274 Robinson, D. G. *et al.* (2015) 'Vesicles versus Tubes: Is Endoplasmic Reticulum-Golgi
1275 Transport in Plants Fundamentally Different from Other Eukaryotes?', *Plant Physiology*.
1276 American Society of Plant Biologists, 168(2), pp. 393–406. doi: 10.1104/PP.15.00124.

1277 Roux, A. *et al.* (2002) 'A minimal system allowing tubulation with molecular motors pulling
1278 on giant liposomes', *Proceedings of the National Academy of Sciences*, 99(8), pp. 5394–5399.
1279 doi: 10.1073/pnas.082107299.

1280 Roux, K. J. *et al.* (2018) 'BioID: A Screen for Protein-Protein Interactions', in *Current*
1281 *Protocols in Protein Science*. Hoboken, NJ, USA: John Wiley & Sons, Inc., p. 19.23.1-
1282 19.23.15. doi: 10.1002/cpps.51.

1283 Saito, K. *et al.* (2009) 'TANGO1 facilitates cargo loading at endoplasmic reticulum exit
1284 sites', *Cell*. 2009/03/10, 136(5), pp. 891–902. doi: S0092-8674(08)01630-9
1285 [pii]10.1016/j.cell.2008.12.025.

1286 Saito, K. *et al.* (2011) 'cTAGE5 mediates collagen secretion through interaction with
1287 TANGO1 at endoplasmic reticulum exit sites', *Mol Biol Cell*. 2011/04/29, 22(13), pp. 2301–
1288 2308. doi: mbc.E11-02-0143 [pii]10.1091/mbc.E11-02-0143.

1289 Saito, K. *et al.* (2014) 'Concentration of Sec12 at ER exit sites via interaction with cTAGE5
1290 is required for collagen export', *Journal of Cell Biology*. doi: 10.1083/jcb.201312062.

1291 Saleem, M. *et al.* (2015) 'A balance between membrane elasticity and polymerization energy
1292 sets the shape of spherical clathrin coats', *Nature Communications*, 6(1), p. 6249. doi:
1293 10.1038/ncomms7249.

1294 Santos, A. J. M. *et al.* (2015) 'TANGO1 recruits ERGIC membranes to the endoplasmic
1295 reticulum for procollagen export', *eLife*. doi: 10.7554/eLife.10982.001.

1296 Sasaki, N. *et al.* (2018) 'cTAGE5 acts as a Sar1 GTPase regulator for collagen export',
1297 *bioRxiv*, p. 452904. doi: 10.1101/452904.

1298 Schmid, F. (2017) 'Physical mechanisms of micro- and nanodomain formation in
1299 multicomponent lipid membranes', *Biochimica et Biophysica Acta (BBA) - Biomembranes*,
1300 1859(4), pp. 509–528. doi: 10.1016/j.bbamem.2016.10.021.

1301 Schroeder, L. K. *et al.* (2019) 'Dynamic nanoscale morphology of the ER surveyed by STED
1302 microscopy.', *The Journal of cell biology*. Rockefeller University Press, 218(1), pp. 83–96.
1303 doi: 10.1083/jcb.201809107.

1304 Sens, P. and Rao, M. (2013) 'Chapter 18 – (Re)Modeling the Golgi', in *Methods in Cell*
1305 *Biology*, pp. 299–310. doi: 10.1016/B978-0-12-417164-0.00018-5.

1306 Sens, P. and Turner, M. S. (2006) 'Budded membrane microdomains as tension regulators',
1307 *Physical Review E*, 73(3), p. 031918. doi: 10.1103/PhysRevE.73.031918.

1308 Trabelsi, S. *et al.* (2008) 'Linactants: Surfactant Analogues in Two Dimensions', *Physical*
1309 *Review Letters*, 100(3), p. 037802. doi: 10.1103/PhysRevLett.100.037802.

1310 Upadhyaya, A. and Sheetz, M. P. (2004) 'Tension in tubulovesicular networks of Golgi and
1311 endoplasmic reticulum membranes.', *Biophysical journal*, 86(5), pp. 2923–8. doi:
1312 10.1016/S0006-3495(04)74343-X.

1313 Venditti, R. *et al.* (2012) 'Sedlin controls the ER export of procollagen by regulating the Sar1
1314 cycle.', *Science (New York, N.Y.)*, 337(6102), pp. 1668–72. doi: 10.1126/science.1224947.

1315 Watson, P. *et al.* (2005) 'Coupling of ER exit to microtubules through direct interaction of

1316 COPII with dynactin.', *Nature cell biology*, 7(1), pp. 48–55. doi: 10.1038/ncb1206.

1317 Wilson, D. G. *et al.* (2011) 'Global defects in collagen secretion in a Mia3/TANGO1
1318 knockout mouse', *J Cell Biol*. 2011/05/25, 193(5), pp. 935–951. doi: jcb.201007162
1319 [pii]10.1083/jcb.201007162.

1320 Wolff, J., Komura, S. and Andelman, D. (2015) 'Budding of domains in mixed bilayer
1321 membranes', *Physical Review E*, 91(1), p. 012708. doi: 10.1103/PhysRevE.91.012708.

1322 Wu, X.-S. *et al.* (2017) 'Membrane Tension Inhibits Rapid and Slow Endocytosis in
1323 Secretory Cells.', *Biophysical journal*, 113(11), pp. 2406–2414. doi:
1324 10.1016/j.bpj.2017.09.035.

1325 Yang, S.-T., Kiessling, V. and Tamm, L. K. (2016) 'Line tension at lipid phase boundaries as
1326 driving force for HIV fusion peptide-mediated fusion', *Nature Communications*, 7(1), p.
1327 11401. doi: 10.1038/ncomms11401.

1328 Yuan, L. *et al.* (2018) 'TANGO1 and SEC12 are copackaged with procollagen I to facilitate
1329 the generation of large COPII carriers', *Proc Natl Acad Sci U S A*, 115(52), pp. E12255–
1330 E12264. doi: 10.1073/pnas.1814810115.

1331 Zanetti, G. *et al.* (2013) 'The structure of the COPII transport-vesicle coat assembled on
1332 membranes', *Elife*. 2013/09/26, 2, p. e00951. doi: 10.7554/eLife.00951.

1333 Zeuschner, D. *et al.* (2006) 'Immuno-electron tomography of ER exit sites reveals the
1334 existence of free COPII-coated transport carriers', *Nature Cell Biology*. Nature Publishing
1335 Group, 8(4), pp. 377–383. doi: 10.1038/ncb1371.

1336

1337

SUPPLEMENTARY INFORMATION

COMPUTATION OF THE PREFERRED ERES SIZE UNDER TANGO1 DEWETTING CONDITIONS

To compute the preferred ERES size independently of TANGO1 interaction, we consider the situation of complete dewetting, $\omega = 0$, which allows us to simplify ***Equation (2)*** in the main text as $\bar{f}(\omega = 0) = \frac{2}{\rho} + \frac{1}{2}\bar{f}_0(\rho - 1)^2$. Under these conditions, energy minimization, corresponding to the solutions of the equation $\frac{\partial \bar{f}(\omega=0)}{\partial \rho}\Big|_{\rho=\rho_{unwett}} = 0$, can be expressed as a third order equation with a real solution for the optimal ERES radius given by

$$\rho_{unwett} = \frac{1}{3}(1 + \Xi + 1/\Xi) \quad : \quad \Xi = \left(1 + \frac{27}{\bar{f}_0} + 3\sqrt{\frac{6}{\bar{f}_0} + \left(\frac{9}{\bar{f}_0}\right)^2}\right)^{1/3}, \qquad \textbf{(S1)}$$

which only depends on the dimensionless coupling factor $\bar{f}_0 = f_0 {R_0}^3/\lambda_0$, and is always larger than 1, since the line tension λ_0 in ***Equation (1)*** in the main text is positive by definition and would always work to reduce the amount of ERES by increasing their size (thus favoring ERES growth).

CRITICAL FILAMENT SPONTANEOUS CURVATURE

Specifically, we computed how the optimal ring size varies as a response to a decrease in the linactant strength (parameter $\overline{\Delta\lambda}$). From ***Equation (4)***, we can calculate the rate of change of the ring radius with respect to changes in $\overline{\Delta\lambda}$. From this, we can see that, for $\rho = 1$, increasing the COPII domain line tension (decreasing the values of $\overline{\Delta\lambda}$), leads to larger rings except for some extreme negative values of the filament spontaneous curvature, smaller than a critical spontaneous curvature, $c_0 < -\frac{3}{2}\left(1 + \frac{f_0}{6\kappa_T}\right) = c_{0,crit}$. However, for such values, the line energy gain associated with the filament wetting the ERES (***Equation (M2)***), is $\Delta F_{line,wett} = \Delta\lambda L$, whereas the free energy loss associated with bending the filament upon wetting (***Equation (M1)***) is $\Delta F_{bend,wett} = \frac{\kappa_T}{2{R_0}^2}\left(\frac{5}{2} + \frac{f_0}{\kappa_T}\right)^2 L$, where we considered the critical spontaneous curvature calculated above. Under these conditions, wetting only occurs if the energy gain due to the line tension decrease is larger than the energy loss upon filament bending, that is, $\Delta F_{line,wett} \geq \Delta F_{bend,wett}$. This implies that $\overline{\Delta\lambda} \geq \frac{1}{2}\overline{\kappa_T}\left(\frac{5}{2} + \frac{\bar{f}_0}{\overline{\kappa_T}}\right)^2$. Since, by definition, $\overline{\Delta\lambda} \leq 1$, there is only a very small range of parameters $\overline{\kappa_T}$ and $\bar{f}_0$, given by $0 \leq \bar{f}_0 \leq -\frac{5\overline{\kappa_T}}{2} + \sqrt{2\overline{\kappa_T}}$, for which there is filament wetting of the COPII patch at spontaneous curvatures smaller than the critical spontaneous curvatures. Hence, according to our model the reduction in ring size in cells expressing TANGO1-ΔPRD as compared to full-length TANGO1-expressing cells can hardly be explained solely by the reduced interaction of the TANGO1 filament with Sec23.

SUPPLEMENTARY FIGURE LEGENDS

Figure S1. Multiple ring geometry.
(A) Description of the ring geometry (of radius R) for neighboring rings, assembled in a hexagonal lattice and separated by a center-to-center distance, a. The COPII components are schematically represented in orange, whereas the wetting TANGO1 filament is shown in blue.

Figure S2. Computed sizes of the TANGO1 rings.
(A-D) Numerically computed phase diagrams showing the wetting-dewetting transitions (solid black lines) as a function of the line tension reduction ($\overline{\Delta\lambda}$) and the dimensionless filament bending rigidity, $\overline{\kappa_T}$, **(A, B)**; the dimensionless coupling factor, $\overline{f_0}$, **(C)**; or the filament spontaneous curvature, $\overline{c_0}$ **(D)**. The parameters are taken as indicates, and in **(A-C)** the filament spontaneous curvature is equal to 0. In the parameter space where wetting is predicted, the optimal ring size, ρ_{ring}, is shown in color code. Dashed lines represent the iso-size lines, and arrows represent possible trajectories in the parameter space allowing for a reduction in the TANGO1 ring size while reducing affinity of TANGO1 filament for COPII subunits.

Figure S3. Geometry and physical forces in the transport intermediate generation model.
(A) TANGO1 rings assembling on the ER membrane are depicted in light blue, accounting for a line tension reduction of the COPII coat, $\Delta\lambda$. The ER membrane is shown in black, associated with a tension, σ_0. The COPII coat polymerizing on the membrane is depicted in orange, and accounts for a coat binding free energy (or chemical potential), μ_c, and a COPII coat line tension, λ_0. Packaged procollagen rods are shown in magenta, which can contribute with a pushing normal force, N. Finally, ERGIC53-containing membranes tethered to the export site through the NRZ complex (dark blue) can lead to a membrane tension reduction, $\Delta\sigma$. **(B)** Scheme of the carrier geometry used for shallow buds *(i)*, deep buds *(ii)*; and pearled carriers *(iii)*. See Materials and Methods for the detailed description of the geometric parameters.

Figure S4. Physical model of TANGO1 ring fusion.
(A) Schematic representation of the pathway leading to fusion of nearby ERES wetted by TANGO1 filaments, as shown in Figure 3A, indicating the main geometric parameters used in our calculations. **(B)** Computed free energy changes (for fusion in orange, for filament breaking in black, and for merge in blue, see the explanatory energy scheme shown in **(A)**), plotted as a function of the dewetting angle. No ring fusion is possible for dewetting angles smaller than a minimal dewetting angle α_{min} (see supplementary text for details). The model parameters used for this plot are designated in the figure. **(C)** Simplified geometry used for the fused ring spreading computations (top), and examples shown for three different β angles (bottom). **(D)** Plot of the free energy of the fused, spread two-ring configuration as a function of the spreading angle, β, showing the angle, β_{opt}, corresponding to the spreading configuration of minimal energy. **(E, F)** Ring merger energy (that is, the barrier for ring fusion minus the filament breaking energy) as a function of the distance between rings, a, **(E)**; and as a function of the dimensionless bending rigidity of the TANGO1 filament **(F)**, for the values of the rest of parameters as shown in the legends of these panels. **(G)** Plot of the free energy change between the separated rings and the fused and spread rings as a function of the ring spontaneous curvature. Positive regions indicate regions where fused rings correspond to locally stable (metastable) states (indicated by the shaded region of the diagram), whereas regions with a negative free energy change indicate globally stable fused rings.